Computers and Mathematics with Applications 71 (2016) 1198–1226

Contents lists available at ScienceDirect

Computers and Mathematics with Applications

journal homepage: www.elsevier.com/locate/camwa

Development of a 3D staggered FDTD scheme for solving Maxwell's equations in Drude medium

Tony W.H. Sheu [a,b,c,*], Y.C. Wang [a], J.H. Li [a]

[a] Department of Engineering Science and Ocean Engineering, National Taiwan University, No. 1, Sec. 4, Roosevelt Road, Taipei, Taiwan, ROC

[b] Center for Advanced Study in Theoretical Sciences (CASTS), National Taiwan University, Taipei, Taiwan, ROC

[c] Institute of Applied Mathematical Sciences, National Taiwan University, Taipei, Taiwan, ROC

ARTICLE INFO

Article history:
Received 22 August 2014
Received in revised form 13 January 2016
Accepted 23 January 2016
Available online 28 February 2016

Keywords:
Maxwell's equations
Staggered grids
Zero-divergence
Symplectic partitioned Runge–Kutta
Fourth-order
Exact and numerical phase velocities

ABSTRACT

An explicit finite-difference scheme is developed to solve the three-dimensional Maxwell's equations in Drude medium. Our aim of developing this scheme in time domain is to compute solutions in staggered grids from the Faraday's and Ampère's equations. The electric and magnetic field solutions are sought subject to the discrete zero-divergence condition (Gauss's law). The local conservation laws in ideal Maxwell's equations are also numerically preserved all the time using the explicit second-order accurate symplectic partitioned Runge–Kutta temporal scheme. The spatial derivative terms in the Faraday's and Ampère's equations are discretized to obtain fourth-order accuracy using the developed scheme underlying the concept of minimizing the discrepancy between the exact and the derived numerical phase velocities. Dispersion and anisotropy errors have been much reduced through the procedure of minimizing phase velocity error. In addition to performing the fundamental analysis on the proposed scheme, the computational efficiency and long-term accurate properties embedded in the proposed symplectic dispersion-error reduction centered scheme are numerically demonstrated through several test problems investigated in ideal and Drude media.

1. Introduction

In Maxwell's equations, Gauss's law is considered as a constraint equation on the Faraday's and Ampère's equations. However, numerically introduced errors of different kinds cause the magnetic and electric fields to no longer be divergence free. The resulting nonzero-divergence error may make the predicted solution less stable when simulating electromagnetic (*EM*) wave propagation. Circumvention of this instability problem has been one of the academically challenging tasks in the development of an efficient solver for solving the Maxwell's equations in ideal or in dispersive medium [1]. Two divergence-free constraint equations in Gauss's law can be numerically satisfied at all times when solving the Maxwell's equations in the currently employed Yee's staggered grid system [2]. The generalized Lagrange multiplier formulation of Munz et al. [3] is also applicable to retain numerical divergence-free condition in the Maxwell's equations. One can compute a local divergence-free Maxwell's solution as well using the discontinuous Galerkin finite element method in [4].

* Corresponding author at: Institute of Applied Mathematical Sciences, National Taiwan University, Taipei, Taiwan, ROC. Tel.: +886 2 33665746; fax: +886 2 23929885.

E-mail address: twhsheu@ntu.edu.tw (T.W.H. Sheu).

http://dx.doi.org/10.1016/j.camwa.2016.01.025
0898-1221/

Numerical methods developed to predict the propagation of *EM* waves can be classified into the integral and differential types. The integral methods include, for example, the method of moments, boundary element method, and fast multipole method. The other more popular differential methods contain the finite difference, finite element, finite volume, pseudospectral, transition line matrix and multiresolution methods. The finite difference method developed in time domain is simple to write a program and is comparatively efficient [2]. Moreover, finite difference and finite element methods can be employed together to yield a hybrid scheme for solving the Maxwell's equations in nonconforming meshes [5]. Therefore, the finite difference time domain (FDTD) method is employed in the present study to approximate Maxwell's equations in staggered grids so as to be able to get the divergence-free electromagnetic field solutions.

While approximating the derivative terms using a differential method, the numerically introduced dissipation error can smear *EM* wave solution and the predicted dispersion error, on the contrary, may result in a wrong phase speed or group velocity [6]. Since the dispersion error can make the scheme less stable, it is essential to develop a dispersion-error reducing method to approximate the first-order spatial derivative terms. Prediction of a correct propagation characteristics constitutes the second objective of the present simulation study of the Maxwell's equations. At late-time of the electromagnetic wave prediction, the solution quality can be deteriorated by the other type of numerical errors generated from the use of non-symplectic temporal schemes. Preservation of the desirable symplectic property in a long-term computation of Maxwell's equations motivated us to properly approximate the time derivative terms shown in the Faraday's and Ampère's equations.

Besides the numerical instability and numerical dispersion error, when simulating Maxwell's equations by finite difference time domain method the so-called anisotropy error is also recognized as a significant source of error since this type of error exhibits accumulative and erroneous propagation characteristics. Dispersive and anisotropy errors may cause unphysical results and mislead researchers into drawing incorrect conclusions. These two important issues in the society of computational electromagnetics need to be addressed in the development of FDTD scheme.

While simulating wave propagation problems in open domains, one needs to truncate the investigated physical domain because of the limited available computational resources in random access memory and in computing time. To overcome this practical problem, the guideline one can adopt is to prescribe a proper boundary condition at users' truncated boarder in the hope of preventing wave reentry into the domain. Otherwise, the outgoing and reflection waves may interact with each other. Such an erroneous wave interaction will contaminate the solution predicted from the Maxwell's equations. Apart from the conventional absorbing boundary operators [7], which can exhibit a large reflection error, and the theoretically exact but computationally more expensive boundary integral method [8], the perfectly matched Layer (PML) method was proposed firstly by Berenger in his split-field formulation [9]. Different refined variants of the absorbing boundary condition such as the stretched coordinate PML [10], anisotropic-medium (uniaxial) PML [11] and complex frequency shifted (CFS) PML [12] developed for truncating boundary in time domain have been successfully applied to simulate EM waves in open domain. Application of PML methods requires no field-splitting [13]. In this study CPML (Convolutional PML) method is adopted to calculate the time dependent solutions from the Maxwell's equations.

The rest of this paper is organized as follows. In Section 2, the Maxwell's equations applicable to model the EM wave in non-dispersive and dispersive media are presented. A solution algorithm presented in Section 3 splits the equations into a part accounting for the ideal Maxwell's equations and the other part responsible for the dispersive Drude medium. The lossless ideal Maxwell's equations are rigorously approximated in space and in time as well. In Section 4, some remarkable features existing in the Maxwell's equations that are essential to develop the current scheme in time domain are reviewed. The explicit symplectic PRK (Partitioned Runge–Kutta) temporal scheme developed to conserve Hamiltonians in the ideal Maxwell's equations is applied. Employment of this non-iterative explicit scheme enables us to derive the numerical dispersion relation equation. The newly developed scheme with the optimized numerical phase velocity feature is also detailed. We will verify the proposed numerical method and then discuss the results predicted in the investigated Drude medium in Section 6. Finally, some concluding remarks are drawn in Section 7.

2. Working equations

The electric permittivity and magnetic permeability are normally varied with the optical frequency in dispersive media. In the current numerical study in time domain, for simplicity only the electric permittivity is assumed to be frequency-dependent. The electric permittivity $\varepsilon(t)$ ($\equiv \varepsilon_r\varepsilon_o$) is assumed to be equal to $(1+\chi)\varepsilon_0$, where ε_r ($\equiv 1+\chi$) is the relative permittivity, $\chi(t)$ is the electric susceptibility, t is the time, and ε_0 is the vacuum permittivity. The susceptibility and the relative electric permittivity are modeled as $\chi(\omega) = -\frac{\omega_p^2}{\omega^2 - j\omega\gamma_p}$, where ω is an angular frequency, or $\chi(t) = \frac{\omega_p^2}{\gamma_p}\left(1 - e^{-\gamma_p t}\right)u(t)$ and $\varepsilon_r(\omega) = \varepsilon_\infty - \frac{\omega_p^2}{\omega^2 - j\omega\gamma_p}$. The constant ε_∞ accounts for the effect of the charged material at high frequencies. As ω goes to infinity, the relative permittivity reduces to ε_∞. The notation $u(t)$ stands for the unit step function. Here, $\omega_p^2 = \frac{NQ^2}{M\varepsilon_0}$. In the Drude model, M denotes the mass of the charge, Q is the amount of charge, and N represents the number of dipoles per unit volume. The notations j and γ_p in the constitutive equation $\chi(\omega)$ denote respectively the imaginary unit and the damping coefficient.

Table 1
Comparison of the equations used in UPML and CPML.

–	UPML	CPML
Time-harmonic Maxwell's equations:	$\nabla \times \underline{H} = j\omega\varepsilon \underline{S}\, \underline{E} = j\omega \underline{\varepsilon} \cdot \underline{E}$ $\nabla \times \underline{E} = -j\omega\mu \underline{S}\, \underline{H} = -j\omega \underline{\mu} \cdot \underline{H}$	$\nabla_s \times \underline{H} = j\omega\varepsilon \underline{E}$ $\nabla_s \times \underline{E} = -j\omega\varepsilon \underline{H}$
Frequency domain:	$j\omega D_x = \frac{1}{s_y}(\frac{\partial H_z}{\partial y} - \frac{\partial H_y}{\partial z})$ $j\omega D_y = \frac{1}{s_z}(\frac{\partial H_x}{\partial z} - \frac{\partial H_z}{\partial x})$ $j\omega D_z = \frac{1}{s_x}(\frac{\partial H_y}{\partial x} - \frac{\partial H_x}{\partial y})$	$j\omega D_x = \frac{1}{s_y}\frac{\partial H_z}{\partial y} - \frac{1}{s_z}\frac{\partial H_y}{\partial z}$ $j\omega D_y = \frac{1}{s_z}\frac{\partial H_x}{\partial z} - \frac{1}{s_x}\frac{\partial H_z}{\partial x}$ $j\omega D_z = \frac{1}{s_x}\frac{\partial H_y}{\partial x} - \frac{1}{s_y}\frac{\partial H_x}{\partial y}$
Parameters:	$S_i = \kappa_i + \frac{\sigma_i}{0+j\omega\varepsilon_0}$ $\kappa_i = 1\ (i = x, y, z)$	$S_i = \kappa_i + \frac{\sigma_i}{a_i+j\omega\varepsilon_0}$ $(i = x, y, z)$

For a medium whose magnetic permeability is frequency independent, the Ampère's and Faraday's laws can be respectively represented in time domain for the electric field variable $\underline{E}$ and the magnetic field variable $\underline{H}$ given below

$$\frac{\partial}{\partial t}(\varepsilon(\underline{x}, t) * \underline{E}(\underline{x}, t)) = \nabla \times \underline{H} - \underline{J}_d, \tag{1}$$

$$\mu \frac{\partial \underline{H}}{\partial t} = -\nabla \times \underline{E}. \tag{2}$$

In Eq. (2), μ is identical to $\mu_0\mu_r$, where μ_0 and μ_r denote the free-space magnetic permeability and the relative magnetic permeability, respectively. The polarization current $\underline{J}_d$ shown in (1) varies with the dispersive optical medium. For simplicity, both of the volume electric and magnetic current densities are assumed to be zero under a source-free condition. The solution of the resulting differential system is sought subject to the Gauss's law, or $\nabla \cdot \underline{B} = \nabla \cdot \underline{D} = 0$. The convolutional operator "$*$" in Eq. (1) is defined as $f(t) * g(t) = \int_0^t f(t-\tau)g(\tau)\, d\tau$ for a set of two arbitrary functions f and g.

The vector equation used for modeling the polarization current is given below for the currently investigated Drude dispersive medium

$$\gamma_p \frac{\partial \underline{J}_d}{\partial t} + \frac{\partial^2 \underline{J}_d}{\partial t^2} = \varepsilon_0 \omega_p^2 \frac{\partial \underline{E}}{\partial t}. \tag{3}$$

In the above, ω_p ($\equiv 2\pi f_p$) is the Drude pole frequency. The inverse of the pole relaxation time is denoted as γ_p ($\equiv 20$ GHz). In the literature, three-dimensional Maxwell's equations have been numerically solved in other types of dispersive media, such as in Debye medium [14–18] and in Lorentz medium [15–18].

When simulating wave propagation, an open domain needs to be truncated so as to make the computation possible. To reduce the amount of unphysical wave reflection from a truncated boundary, a convolutional perfectly matched layer (CPML) of finite width is attached to the truncated domain to absorb the reflected wave. The TM-mode Maxwell's equations in this absorbing layer are as follows in time domain [19]

$$\begin{aligned}
\frac{\partial E_x}{\partial t} &= \frac{1}{\varepsilon_0\varepsilon_r}\left(\frac{1}{k_y}\frac{\partial H_z}{\partial y} - \frac{1}{k_z}\frac{\partial H_y}{\partial z} - J_{d,x} + \psi_{E_{x,y}} - \psi_{E_{x,z}}\right),\\
\frac{\partial E_y}{\partial t} &= \frac{1}{\varepsilon_0\varepsilon_r}\left(\frac{1}{k_z}\frac{\partial H_x}{\partial z} - \frac{1}{k_x}\frac{\partial H_z}{\partial x} - J_{d,y} + \psi_{E_{y,z}} - \psi_{E_{y,x}}\right),\\
\frac{\partial E_z}{\partial t} &= \frac{1}{\varepsilon_0\varepsilon_r}\left(\frac{1}{k_x}\frac{\partial H_y}{\partial x} - \frac{1}{k_y}\frac{\partial H_x}{\partial y} - J_{d,z} + \psi_{E_{z,x}} - \psi_{E_{z,y}}\right),\\
\frac{\partial H_x}{\partial t} &= -\frac{1}{\mu_0\mu_r}\left(\frac{1}{k_y}\frac{\partial E_z}{\partial y} - \frac{1}{k_z}\frac{\partial E_y}{\partial z} + \psi_{H_{x,y}} - \psi_{H_{x,z}}\right),\\
\frac{\partial H_y}{\partial t} &= -\frac{1}{\mu_0\mu_r}\left(\frac{1}{k_z}\frac{\partial E_x}{\partial z} - \frac{1}{k_x}\frac{\partial E_z}{\partial x} + \psi_{H_{y,z}} - \psi_{H_{y,x}}\right),\\
\frac{\partial H_z}{\partial t} &= -\frac{1}{\mu_0\mu_r}\left(\frac{1}{k_x}\frac{\partial E_y}{\partial x} - \frac{1}{k_y}\frac{\partial E_x}{\partial y} + \psi_{H_{z,x}} - \psi_{H_{z,y}}\right).
\end{aligned} \tag{4}$$

In the above, k_i ($i = x, y, z$) denotes the wavenumber along the i-direction. The notation $\psi_{w,v}$ is defined as $\zeta_w(t) * \partial H_v(t)/\partial w$, where $\zeta_w(t) * \partial H_v(t)/\partial w$ or $\zeta_w(t) * \partial E_v(t)/\partial w$ ($w = x, y, z$; $v = x, y, z$) stands for the convolutional term. The TM-mode Maxwell's equations in CPML as well as in UPML are summarized in Table 1 for completeness.

To reduce the computational time of calculating the absorption terms $\psi^n_{E_{x,y}}$, $\psi^n_{E_{x,z}}$ $\psi^n_{E_{y,x}}$, $\psi^n_{E_{y,z}}$ $\psi^n_{E_{z,x}}$, $\psi^n_{E_{z,y}}$, $\psi^{n+\frac{1}{2}}_{H_{x,y}}$ $\psi^{n+\frac{1}{2}}_{H_{x,z}}$ $\psi^{n+\frac{1}{2}}_{H_{y,x}}$ $\psi^{n+\frac{1}{2}}_{H_{y,z}}$ $\psi^{n+\frac{1}{2}}_{H_{z,x}}$ and $\psi^{n+\frac{1}{2}}_{H_{z,y}}$, one can approximate them by $\psi^n_{E_{x,y}} = b_y \cdot \psi^{n-1}_{E_{x,y}} + c_y \cdot \frac{\partial H^n_z}{\partial y}$, $\psi^n_{E_{x,z}} = b_z \cdot \psi^{n-1}_{E_{x,z}} + c_z \cdot \frac{\partial H^n_y}{\partial z}$,

$\psi^n_{E_{y,x}} = b_x \cdot \psi^{n-1}_{E_{y,x}} + c_x \cdot \frac{\partial H^n_z}{\partial x}$, $\psi^n_{E_{y,z}} = b_z \cdot \psi^{n-1}_{E_{y,z}} + c_z \cdot \frac{\partial H^n_x}{\partial z}$, $\psi^n_{E_{z,x}} = b_x \cdot \psi^{n-1}_{E_{z,x}} + c_x \cdot \frac{\partial H^n_y}{\partial x}$, $\psi^n_{E_{z,y}} = b_y \cdot \psi^{n-1}_{E_{z,y}} + c_y \cdot \frac{\partial H^n_x}{\partial y}$,
$\psi^{n+\frac{1}{2}}_{H_{x,y}} = b_y \cdot \psi^{n-\frac{1}{2}}_{H_{x,y}} + c_y \cdot \frac{\partial E^{n+\frac{1}{2}}_z}{\partial y}$, $\psi^{n+\frac{1}{2}}_{H_{x,z}} = b_z \cdot \psi^{n-\frac{1}{2}}_{H_{x,z}} + c_z \cdot \frac{\partial E^{n+\frac{1}{2}}_y}{\partial z}$, $\psi^{n+\frac{1}{2}}_{H_{y,x}} = b_x \cdot \psi^{n-\frac{1}{2}}_{H_{y,x}} + c_x \cdot \frac{\partial E^{n+\frac{1}{2}}_z}{\partial x}$, $\psi^{n+\frac{1}{2}}_{H_{y,z}} = b_z \cdot \psi^{n-\frac{1}{2}}_{H_{y,z}} + c_z \cdot \frac{\partial E^{n+\frac{1}{2}}_x}{\partial z}$,
$\psi^{n+\frac{1}{2}}_{H_{z,x}} = b_x \cdot \psi^{n-\frac{1}{2}}_{H_{z,x}} + c_x \cdot \frac{\partial E^{n+\frac{1}{2}}_y}{\partial x}$, $\psi^{n+\frac{1}{2}}_{H_{z,y}} = b_y \cdot \psi^{n-\frac{1}{2}}_{H_{z,y}} + c_y \cdot \frac{\partial E^{n+\frac{1}{2}}_x}{\partial y}$. The coefficients b_w and c_w are given below

$$b_w = e^{\left(-\left(\frac{\sigma_w}{\varepsilon_0 k_w} + \frac{a_w}{\varepsilon_0}\right)\Delta t\right)};$$
$$c_w = \frac{\sigma_w}{\sigma_w k_w + k_w^2 a_w}\left(e^{\left(-\left(\frac{\sigma_w}{\varepsilon_0 k_w} + \frac{a_w}{\varepsilon_0}\right)\Delta t\right)} - 1\right); \quad w = x, y, z. \tag{5}$$

The subscript w denotes x, y or z and $\sigma_w = \sigma_{\max}\left(\frac{d-w}{d}\right)^m$, $a_w = a_{\max}\left(\frac{d-w}{d}\right)^{m_a}$, $k_w = 1 + (k_{\max} - 1)\cdot\left(\frac{d-w}{d}\right)^m$.

3. Solution algorithm

The equations shown in (4) consist of the ideal Maxwell's equations, polarization current term J_d, and the absorption term added only to the convolutional perfectly matched layer. The quality of simulating wave propagation in Drude medium, characterized by the constitutive equation for the relative electric permittivity ε_r, depends partly on the scheme employed to solve the Maxwell's equations in free space. This chosen constitutive equation is also essential since it determines the simulation quality on the polarization current. In addition, the convolutional terms shown in the CPML equations should be able to absorb the possibly reflected waves from the truncated boundary. The entire set of equations in (4) is therefore decomposed into the ideal Maxwell's equations, the constitutive equation for modeling the terms related to the Drude medium, the polarization current for the optical medium, and the prescribed wave absorption coefficient in CPML. It is therefore legitimate for us to solve them separately using their respective suitable numerical methods.

Besides the numerical methods employed to calculate the absorption terms and the polarization current, the solution quality predicted from the wave equations in Drude medium depends highly on the scheme, detailed in Section 4, developed for the approximation of Maxwell's equations in vacuum

$$\begin{aligned}
\frac{\partial E_x}{\partial t} &= \frac{1}{\varepsilon_0\varepsilon_r}\left(\frac{1}{k_y}\frac{\partial H_z}{\partial y} - \frac{1}{k_z}\frac{\partial H_y}{\partial z}\right),\\
\frac{\partial E_y}{\partial t} &= \frac{1}{\varepsilon_0\varepsilon_r}\left(\frac{1}{k_z}\frac{\partial H_x}{\partial z} - \frac{1}{k_x}\frac{\partial H_z}{\partial x}\right),\\
\frac{\partial E_z}{\partial t} &= \frac{1}{\varepsilon_0\varepsilon_r}\left(\frac{1}{k_x}\frac{\partial H_y}{\partial x} - \frac{1}{k_y}\frac{\partial H_x}{\partial y}\right),\\
\frac{\partial H_x}{\partial t} &= -\frac{1}{\mu_0\mu_r}\left(\frac{1}{k_y}\frac{\partial E_z}{\partial y} - \frac{1}{k_z}\frac{\partial E_y}{\partial z}\right),\\
\frac{\partial H_y}{\partial t} &= -\frac{1}{\mu_0\mu_r}\left(\frac{1}{k_z}\frac{\partial E_x}{\partial z} - \frac{1}{k_x}\frac{\partial E_z}{\partial x}\right),\\
\frac{\partial H_z}{\partial t} &= -\frac{1}{\mu_0\mu_r}\left(\frac{1}{k_x}\frac{\partial E_y}{\partial x} - \frac{1}{k_y}\frac{\partial E_x}{\partial y}\right).
\end{aligned} \tag{6}$$

The necessity of applying a symplectic temporal discretization scheme is described in Section 4 so as to preserve the symplectic structure existing in the above Hamiltonian differential system. One needs also to optimize the numerical dispersion relation equation described in Section 5 to correctly approximate the first-order spatial derivative terms. In the current *EM* wave simulation, another objective of this study is to rigorously determine the users' prescribed values of Δt and Δx in the sense that numerical dispersion relation equations for the Ampère's and Faraday's equations are satisfied at each nodal point in the physical domain.

4. Numerical methods for ideal Maxwell's equations

Maxwell's equations in the ideal medium can be represented in the following curl form for the field variables $\underline{E} = \left(E_x, E_y, E_z\right)^T$ and $\underline{H} = \left(H_x, H_y, H_z\right)^T$

$$\frac{\partial \underline{H}}{\partial t} = -\frac{1}{\mu}\nabla \times \underline{E}, \tag{7}$$
$$\frac{\partial \underline{E}}{\partial t} = \frac{1}{\varepsilon}\nabla \times \underline{H}. \tag{8}$$

The above differential system of Maxwell's equations defined in vacuum has been known as one of the most important Hamiltonian equations and has many mathematically intriguing properties. Inclusion of these distinguished properties in the scheme development plays a key role of determining the quality of the predicted finite difference solution in time domain.

Eqs. (7)–(8) constitute a bi-Hamiltonian differential system. One of the infinite-dimensional Hamiltonian system of Eqs. (1)–(2) is written as $\frac{\delta H_1}{\delta \underline{H}} = \frac{1}{\varepsilon}\nabla \times \underline{H}$ and $\frac{\delta H_1}{\delta \underline{E}} = \frac{1}{\mu}\nabla \times \underline{E}$. The helicity Hamiltonian H_1 is given below [20]

$$H_1 = \frac{1}{2}\int \frac{1}{\varepsilon}\underline{H}\cdot\nabla\times\underline{H} + \frac{1}{\mu}\underline{E}\cdot\nabla\times\underline{E}\, d\Omega. \tag{9}$$

The other Hamiltonian system of Maxwell's equations $\left(\frac{\partial \underline{H}}{\partial t}, \frac{\partial \underline{E}}{\partial t}\right)^T = \underline{\underline{D_2}}\left(\frac{\delta H_2}{\delta \underline{H}}, \frac{\delta H_2}{\delta \underline{E}}\right)^T$, where $\underline{\underline{D_2}}$ is the skew-adjoint matrix $\begin{pmatrix} \underline{0} & -\frac{1}{\varepsilon\mu}\nabla\times \\ \frac{1}{\varepsilon\mu}\nabla\times & \underline{0} \end{pmatrix}$, involves the quadratic Hamiltonian (or energy density) given below [21]

$$H_2 = \frac{1}{2}\int \mu\underline{H}\cdot\underline{H} + \varepsilon\underline{E}\cdot\underline{E}\, d\Omega. \tag{10}$$

4.1. Discrete divergence-free formulation of Maxwell's equations

Three Faraday's equations, three Ampère's equations, and two Gauss's equations constitute a complete system of the three-dimensional Maxwell's equations. In this system of eight differential equations, we need to neglect any two of the eight equations so as to uniquely compute a total number of six solutions for $\underline{E}$ and $\underline{H}$. Gauss's law is normally not taken into consideration since the divergence-free equations for $\underline{H}$ and $\underline{E}$ can be derived analytically from the Faraday's law and Ampère's law, respectively, within the continuous context.

Calculation of the EM wave solution solely from the Faraday's and Ampère's equations may cause the magnetic and electric field equations to no longer satisfy the two divergence free conditions. Provided that the predicted values of $\nabla\cdot\underline{H}$ and $\nabla\cdot\underline{E}$ are not identical to zero any longer, the resulting two predicted incorrect forces that are in parallel with the EM field [22] can in turn produce misleading results. One standard way of circumventing this simulation problem is to carry out calculation in the currently chosen staggered grids. The other way of overcoming the computational difficulty resulting from the omission of Gauss's law while solving the Maxwell's equations is to force the magnetic and electric divergences towards zero through, for example, the use of two properly introduced gradient terms [23–25].

4.2. Explicit symplectic partitioned Runge–Kutta temporal scheme

Since Faraday's and Ampère's equations shown in (7)–(8) constitute a Hamiltonian differential system, we need to numerically preserve the symplectic structure and conserve the total energy. Either an implicit or an explicit symplectic method can be adopted to integrate the currently investigated infinite dimensional Hamiltonian system of canonical equations. In addition to preserving the existing symplectic structure, we also aim to develop a very accurate spatial scheme by forcing the numerical dispersion relation equation for the Maxwell's equations to be closer to the exact dispersion relation equation. In wavenumber space, we therefore need to derive the numerical angular frequency in terms of the wavenumbers. Sanz-Serna [26] demonstrated that it is impossible to apply any implicit symplectic Runge–Kutta scheme to derive an explicit form of the numerical dispersion relation equation. The explicit-type symplectic Runge–Kutta scheme is therefore employed in this study so that the discrepancy between the exact and numerical phase velocities can be minimized when solving the separable Hamiltonian system of Maxwell's equations.

The second-order accurate explicit symplectic partitioned Runge–Kutta scheme presented in [27] is adopted here to approximate the time derivative terms

$$\underline{H}^{n+\frac{1}{2}} = \underline{H}^n - \frac{dt}{2\mu}\nabla\times\underline{E}^n, \tag{11}$$

$$\underline{E}^{n+1} = \underline{E}^n + \frac{dt}{\varepsilon}\nabla\times\underline{H}^{n+\frac{1}{2}}, \tag{12}$$

$$\underline{H}^{n+1} = \underline{H}^{n+\frac{1}{2}} - \frac{dt}{2\mu}\nabla\times\underline{E}^{n+1}. \tag{13}$$

When constructing a numerical scheme for the long time computation of Maxwell's equations in lossless medium without sources, one should conserve energy to retain the physical features. To keep the density of the electromagnetic energy of wave to be constant, one can apply different ideas to achieve the goal using either the splitting FDTD methods proposed in [28] or applying the energy-conserved method of Gao and Liang [29].

4.3. Approximation of the spatial derivative terms

When applying the finite difference method to solve the hyperbolic Maxwell's equations in time domain, we need to reduce numerical errors of the dispersion and anisotropy types [30]. The spatial derivative terms shown in (11)–(13) will be approximated underlying the modified equation analysis and the dispersion analysis.

According to Eq. (13), at $t = n\Delta t$ one can get $\underline{H}^n = \underline{H}^{n-\frac{1}{2}} - \frac{dt}{2\mu}\nabla \times \underline{E}^n$. This equation for $\underline{H}^n$ is then substituted into (11) to yield $\underline{H}^{n+\frac{1}{2}} = \underline{H}^{n-\frac{1}{2}} - \frac{dt}{2\mu}\nabla \times \underline{E}^n$. From Eq. (12) the equation $\underline{E}^{n+\frac{1}{2}} = \underline{E}^{n-\frac{1}{2}} + \frac{dt}{\varepsilon}\nabla \times \underline{H}^n$ is derived. The semi-discretized Ampere's vector equation has the following three component equations

$$E_z^{n+\frac{1}{2}} = E_z^{n-\frac{1}{2}} + \frac{\Delta t}{\varepsilon}\left(\frac{\partial H_y^n}{\partial x} - \frac{\partial H_x^n}{\partial y}\right), \tag{14a}$$

$$E_x^{n+\frac{1}{2}} = E_x^{n-\frac{1}{2}} + \frac{\Delta t}{\varepsilon}\left(\frac{\partial H_z^n}{\partial y} - \frac{\partial H_y^n}{\partial z}\right), \tag{14b}$$

$$E_y^{n+\frac{1}{2}} = E_y^{n-\frac{1}{2}} + \frac{\Delta t}{\varepsilon}\left(\frac{\partial H_x^n}{\partial z} - \frac{\partial H_z^n}{\partial x}\right). \tag{14c}$$

The dispersive error will be minimized in this study by minimizing the difference between the exact and optimizing numerical dispersion relations. Towards this perspective, we resort to the classical finite difference equations rather than to the implicit type of the compact difference schemes. In staggered grids, the first-order derivative terms $\frac{\partial H_y^n}{\partial x}$ and $\frac{\partial H_x^n}{\partial y}$ at each interior node (i, j, k) are approximated as

$$\begin{aligned}\left.\frac{\partial H_y}{\partial x}\right|_{i,j,k+\frac{1}{2}}^n &= \frac{1}{h}\Big[a_1\left(H_y|_{i+\frac{5}{2},j,k+\frac{1}{2}}^n - H_y|_{i-\frac{5}{2},j,k+\frac{1}{2}}^n\right) + a_2\left(H_y|_{i+\frac{3}{2},j,k+\frac{1}{2}}^n - H_y|_{i-\frac{3}{2},j,k+\frac{1}{2}}^n\right)\\ &\quad + a_3\left(H_y|_{i+\frac{1}{2},j,k+\frac{1}{2}}^n - H_y|_{i-\frac{1}{2},j,k+\frac{1}{2}}^n\right)\Big],\end{aligned} \tag{15a}$$

$$\begin{aligned}\left.\frac{\partial H_x}{\partial y}\right|_{i,j,k+\frac{1}{2}}^n &= \frac{1}{h}\Big[a_1\left(H_x|_{i,j+\frac{5}{2},k+\frac{1}{2}}^n - H_x|_{i,j-\frac{5}{2},k+\frac{1}{2}}^n\right) + a_2\left(H_x|_{i,j+\frac{3}{2},k+\frac{1}{2}}^n - H_y|_{i,j-\frac{3}{2},k+\frac{1}{2}}^n\right)\\ &\quad + a_3\left(H_x|_{i,j+\frac{1}{2},k+\frac{1}{2}}^n - H_x|_{i,j-\frac{1}{2},k+\frac{1}{2}}^n\right)\Big].\end{aligned} \tag{15b}$$

After substituting the Eqs. (15a), (15b) into (14a) and performing Taylor series expansion with respect to E_z at the node $(i, j, k+\frac{1}{2})$, we can get

$$\begin{aligned}&\left.\frac{\partial E_z}{\partial t}\right|_{i,j,k+\frac{1}{2}}^n + \frac{dt^2}{24}\left.\frac{\partial^3 E_z}{\partial t^3}\right|_{i,j,k+\frac{1}{2}}^n + \frac{dt^4}{1920}\left.\frac{\partial^5 E_z}{\partial t^5}\right|_{i,j,k+\frac{1}{2}}^n + \frac{dt^6}{322560}\left.\frac{\partial^7 E_z}{\partial t^7}\right|_{i,j,k+\frac{1}{2}}^n + \cdots\\ &= \frac{1}{\varepsilon}\Bigg\{\Bigg[\left(5a_1 + 3a_2 + a_3\right)\left.\frac{\partial H_y}{\partial x}\right|_{i,j,k+\frac{1}{2}}^n + \left(\frac{125}{24}a_1 + \frac{9}{8}a_2 + \frac{1}{24}a_3\right)dx^2\left.\frac{\partial^3 H_y}{\partial x^3}\right|_{i,j,k+\frac{1}{2}}^n\\ &\quad + \left(\frac{625}{384}a_1 + \frac{81}{640}a_2 + \frac{1}{1920}a_3\right)dx^4\left.\frac{\partial^5 H_y}{\partial x^5}\right|_{i,j,k+\frac{1}{2}}^n + \left(\frac{15625}{64512}a_1 + \frac{243}{35840}a_2 + \frac{1}{322560}a_3\right)dx^6\left.\frac{\partial^7 H_y}{\partial x^7}\right|_{i,j,k+\frac{1}{2}}^n\\ &\quad + \cdots\Bigg] - \Bigg[\left(5a_1 + 3a_2 + a_3\right)\left.\frac{\partial H_y}{\partial x}\right|_{i,j,k+\frac{1}{2}}^n + \left(\frac{125}{24}a_1 + \frac{9}{8}a_2 + \frac{1}{24}a_3\right)dx^2\left.\frac{\partial^3 H_y}{\partial x^3}\right|_{i,j,k+\frac{1}{2}}^n\\ &\quad + \left(\frac{625}{384}a_1 + \frac{81}{640}a_2 + \frac{1}{1920}a_3\right)dx^4\left.\frac{\partial^5 H_y}{\partial x^5}\right|_{i,j,k+\frac{1}{2}}^n + \left(\frac{15625}{64512}a_1 + \frac{243}{35840}a_2 + \frac{1}{322560}a_3\right)dx^6\left.\frac{\partial^7 H_y}{\partial x^7}\right|_{i,j,k+\frac{1}{2}}^n\\ &\quad + \cdots\Bigg]\Bigg\}.\end{aligned} \tag{16}$$

The weighting coefficients a_1, a_2 and a_3 shown above will be determined through the modified equation analysis and the dispersion analysis described below.

Higher order temporal terms $\frac{\partial^3 E_z}{\partial t^3}$, $\frac{\partial^5 E_z}{\partial t^5}$, $\frac{\partial^7 E_z}{\partial t^7}\ldots$ are rewritten to their equivalent spatial derivative terms through the Ampère's equations $\frac{\partial E_z}{\partial t} = \frac{1}{\varepsilon}\left(\frac{\partial H_y}{\partial x} - \frac{\partial H_x}{\partial y}\right)$, $\frac{\partial E_x}{\partial t} = \frac{1}{\varepsilon}\left(\frac{\partial H_z}{\partial y} - \frac{\partial H_y}{\partial z}\right)$, and $\frac{\partial E_y}{\partial t} = \frac{1}{\varepsilon}\left(\frac{\partial H_x}{\partial z} - \frac{\partial H_z}{\partial x}\right)$, thereby yielding the corresponding equations for $\frac{\partial^i E_j}{\partial t^i}$ ($i = 3$ and 5, $j = x, y, z$). By substituting the temporal derivative terms $\frac{\partial^3 E_z}{\partial t^3}$ and $\frac{\partial^5 E_z}{\partial t^5}$

into Eq. (16) and then comparing the resulting equation with the equation $\frac{\partial E_z}{\partial t} = \frac{1}{\varepsilon}\left(\frac{\partial H_y}{\partial x} - \frac{\partial H_x}{\partial y}\right)$, we can get two algebraic equations for a_1, a_2 and a_3, which are

$$5a_1 + 3a_2 + a_3 = 1, \tag{17}$$

and

$$\frac{125}{24}a_1 + \frac{9}{8}a_2 + \frac{1}{24}a_3 - \frac{Cr^2}{24}(5a_1 + 3a_2 + a_3) = 0. \tag{18}$$

In the above, the Courant number is defined by $Cr = \frac{c\Delta t}{h}$ where $h = \Delta x = \Delta y = \Delta z$ denotes the uniform grid spacing. The algebraic equations can be similarly derived from (14b) and (14c), respectively. Three introduced weighting coefficients need to be derived by virtue of the dispersion analysis. Our goal is to derive the numerical dispersion relation equation and take it as the third algebraic equation for an unique determination of a_i $(i = 1, 2, 3)$.

By applying the curl operator on both hand sides of the Faraday's equations and then substituting the resulting equations into the Ampère's equations, the second-order wave equation for $\underline{E}$ as $\frac{1}{c^2}\frac{\partial^2 \underline{E}}{\partial t^2} = \frac{\partial^2 \underline{E}}{\partial x^2} + \frac{\partial^2 \underline{E}}{\partial y^2} + \frac{\partial^2 \underline{E}}{\partial z^2}$ can be derived. By substituting the plane wave solution $\underline{E} = \underline{E}_0 \exp\left(I\left(k_x i\Delta x + k_y j\Delta y + k_z k\Delta z - \omega n\Delta t\right)\right)$ into the equation for $\frac{\partial \underline{E}}{\partial t}|^n_{i,j,k+\frac{1}{2}}$, one can get $\frac{\partial \underline{E}}{\partial t} = -I\frac{2\sin\left(\frac{\omega\Delta t}{2}\right)}{\Delta t}\underline{E}$,

$$\frac{\partial \underline{E}}{\partial x} = 2I\frac{a_1\sin\left(\frac{5}{2}k_x\Delta x\right) + a_2\sin\left(\frac{3}{2}k_x\Delta x\right) + a_3\sin\left(\frac{1}{2}k_x\Delta x\right)}{\Delta x}\underline{E},$$

$$\frac{\partial \underline{E}}{\partial y} = 2I\frac{a_1\sin\left(\frac{5}{2}k_y\Delta y\right) + a_2\sin\left(\frac{3}{2}k_y\Delta y\right) + a_3\sin\left(\frac{1}{2}k_y\Delta y\right)}{\Delta y}\underline{E},$$

$$\frac{\partial \underline{E}}{\partial z} = 2I\frac{a_1\sin\left(\frac{5}{2}k_z\Delta z\right) + a_2\sin\left(\frac{3}{2}k_z\Delta z\right) + a_3\sin\left(\frac{1}{2}k_z\Delta z\right)}{\Delta z}\underline{E},$$

$$\frac{\partial^2 \underline{E}}{\partial t^2} = 4\left(\frac{2\sin\left(\frac{\omega\Delta t}{2}\right)}{\Delta t}\right)^2\underline{E},$$

$$\frac{\partial^2 \underline{E}}{\partial x^2} = -4\left(\frac{a_1\sin\left(\frac{5}{2}k_x\Delta x\right) + a_2\sin\left(\frac{3}{2}k_x\Delta x\right) + a_3\sin\left(\frac{1}{2}k_x\Delta x\right)}{\Delta x}\right)^2\underline{E},$$

$$\frac{\partial^2 \underline{E}}{\partial y^2} = -4\left(\frac{a_1\sin\left(\frac{5}{2}k_y\Delta y\right) + a_2\sin\left(\frac{3}{2}k_y\Delta y\right) + a_3\sin\left(\frac{1}{2}k_y\Delta y\right)}{\Delta y}\right)^2\underline{E},$$

$\frac{\partial^2 \underline{E}}{\partial z^2} = -4\left(\frac{a_1\sin\left(\frac{5}{2}k_z\Delta z\right) + a_2\sin\left(\frac{3}{2}k_z\Delta z\right) + a_3\sin\left(\frac{1}{2}k_z\Delta z\right)}{\Delta z}\right)^2\underline{E}$. The numerical dispersion relation equation can be derived as follows by substituting all the above equations into the second-order wave equation for $\underline{E}$

$$\begin{aligned}\frac{1}{c^2}\frac{\omega^2}{4}\left(\frac{\sin(\omega\Delta t/2)}{\omega\Delta t}\right)^2 = {} & k_x^2\left(\frac{5}{2}a_1\frac{\sin\left(\frac{5}{2}k_x\Delta x\right)}{\frac{5}{2}k_x\Delta x} + \frac{3}{2}a_2\frac{\sin\left(\frac{3}{2}k_x\Delta x\right)}{\frac{3}{2}k_x\Delta x} + \frac{1}{2}a_3\frac{\sin\left(\frac{1}{2}k_x\Delta x\right)}{\frac{1}{2}k_x\Delta x}\right)^2 \\ & + k_y^2\left(\frac{5}{2}a_1\frac{\sin\left(\frac{5}{2}k_y\Delta y\right)}{\frac{5}{2}k_y\Delta y} + \frac{3}{2}a_2\frac{\sin\left(\frac{3}{2}k_y\Delta y\right)}{\frac{3}{2}k_y\Delta y} + \frac{1}{2}a_3\frac{\sin\left(\frac{1}{2}k_y\Delta y\right)}{\frac{1}{2}k_y\Delta y}\right)^2 \\ & + k_z^2\left(\frac{5}{2}a_1\frac{\sin\left(\frac{5}{2}k_z\Delta z\right)}{\frac{5}{2}k_z\Delta z} + \frac{3}{2}a_2\frac{\sin\left(\frac{3}{2}k_z\Delta z\right)}{\frac{3}{2}k_z\Delta z} + \frac{1}{2}a_3\frac{\sin\left(\frac{1}{2}k_z\Delta z\right)}{\frac{1}{2}k_z\Delta z}\right)^2.\end{aligned} \tag{19}$$

The exact dispersion relation equation can be similarly derived by substituting the plane wave solution into the second-order wave equation $\frac{\partial^2 \underline{E}}{\partial t^2} = c^2\nabla^2\underline{E}$, thereby yielding $\left(\frac{\omega}{c}\right)^2 = k_x^2 + k_y^2 + k_z^2$. The wavenumber vector is denoted as $\underline{k} = \left(k_x, k_y, k_z\right)$.

To get an accurate propagation characteristics of the Maxwell's equations, it is essential to reduce numerical error of the dispersion type as much as possible. The reason is that this type of errors can cause the numerical phase velocity to become the function of frequency and propagation angle. The strategy we employ to derive the last required algebraic equation is to make the derived numerical phase velocity to agree perfectly with its exact counterpart. To this end, we can match either the numerical and exact phase velocity $\underline{v}_p$ $(\equiv \frac{\omega_{num}}{\underline{k}})$ or group velocity $\underline{v}_g$ $(\equiv \frac{\partial\omega_{num}}{\partial\underline{k}})$. In this study the difference between the exact phase velocity and the derived numerical phase velocity is minimized. Following this line of thought, we define the

error function as $\left[|\frac{\omega_{num}}{\underline{k}}| - |\frac{\omega_{exact}}{\underline{k}}|\right]^2$ and this error is then minimized in the following weak sense within the integral range of $-m_p\pi \le h\underline{k} \le m_p\pi$

$$E_p = \int_{-m_p\pi}^{m_p\pi} \left[\left|\frac{\omega_{num}}{\underline{k}}\right| - \left|\frac{\omega_{exact}}{\underline{k}}(\equiv c)\right|\right]^2 W_p\, d(k_x\Delta x)\, d(k_y\Delta y)\, d(k_z\Delta z). \tag{20}$$

In the above, $k_x\Delta x$, $k_y\Delta y$ and $k_z\Delta z$ denote the scaled (or modified) wavenumbers along x, y and z directions, respectively. The weighting function W_p introduced to the above minimization procedure enables us to integrate the above equation exactly. The parameter m_p whose value lies between 0 and $\frac{1}{2}$ is included for the purpose of reducing aliasing error.

The value of E_p is minimized by enforcing the limiting condition given by $\frac{\partial E_p}{\partial a_3} = 0$. Through this minimization procedure, the third algebraic equation for a_1, a_2 and a_3 is derived as follows

$$\begin{aligned} &+ 0.013462\, a_3^2 a_1 + 0.024686\, a_2^3 - 0.003317\, a_2 - 0.004562\, a_1 + 0.075261\, a_1 a_2 a_3 \\ &+ 0.105823\, a_1 a_2^2 + 0.078272\, a_1^3 + 0.001195\, a_3^3 + 0.155929\, a_1^2 a_2 + 0.054814\, a_1^2 a_3 \\ &+ 0.026761\, a_3 a_2^2 + 0.009749\, a_3^2 a_2 - 0.001222\, a_3 = 0. \end{aligned} \tag{21}$$

Eq. (21) derived from the above procedure of optimizing the dispersive accuracy is used together with the other two algebraic equations derived previously from the modified equation analysis of second kind. Through a series of calculations, the best result is obtained at $m_p = \frac{1}{2}$. The resulting three introduced coefficients in Eq. (13) are obtained as $a_1 = -0.0002985$, $a_2 = -0.0385073$ and $a_3 = 1.1170147$. By virtue of the minimization procedure implemented in wavenumber space and the modified equation analysis of second kind for $\frac{\partial H_x}{\partial x}$, the proposed space centered scheme is shown to have the spatial accuracy order of four thanks to the derived modified equation $\frac{\partial H_x}{\partial x} = \frac{\partial H_x}{\partial x}|_{exact} - 0.00489575h^4\frac{\partial^5 H_x}{\partial x^5} + O(h^6) + \cdots$.

5. Fundamental analyses of the scheme

Analysis of the proposed symplecticity-preserving explicit scheme endowed with the optimized numerical phase velocity for the Maxwell's equations will be conducted through the Von Neumann stability analysis detailed in Section 5.1, the anisotropy analysis given in Section 5.2, and the dispersion analysis in Section 5.3. Both stability and phase error in FDTD scheme for Maxwell's equations in dispersive dielectrics have been analyzed in [31].

5.1. Von Neumann stability analysis

The stability condition imposed on the proposed explicit scheme is derived by scaling the field variables according to $\underline{E} = \sqrt{\frac{\mu}{\varepsilon}}\underline{E}^*$ and $\underline{H} = \sqrt{\frac{\varepsilon}{\mu}}\underline{H}^*$. We can then rewrite Eqs. (7)–(8) for $\underline{V} = \underline{H}^* + I\underline{E}^*$, where $I = (-1)^{1/2}$, in the normalized space as $\frac{1}{c}\frac{\partial \underline{V}}{\partial t} = I\nabla \times \underline{V}$. The superscript "$*$" has been omitted for the sake of simplicity. Note that $c = \frac{1}{\sqrt{\varepsilon\mu}}$ and this equation holds at $\mu = \varepsilon = 1$.

Following the work detailed in [32], the scaled equation can be rewritten to the equivalent eigenvalue equations $\frac{\partial \underline{V}}{\partial t} = \lambda\underline{V}$ and $Ic\nabla \times \underline{V} = \lambda\underline{V}$. The term $\frac{\partial \underline{V}}{\partial t}$ is approximated as $\underline{V}^{n+\frac{1}{2}} - \underline{V}^{n-\frac{1}{2}} = \lambda\Delta t\underline{V}^n$ using the symplectic PRK temporal scheme described in Section 3.1. Define the amplification factor as $G = \left|\frac{\underline{V}^{n+\frac{1}{2}}}{\underline{V}^n}\right|$, one can easily derive $G^2 - (\lambda\Delta t)\, G - 1 = 0$, from which we can get $G_{1,2} = \frac{\lambda\Delta t}{2} \pm \left(1 + \left(\frac{\lambda\Delta t}{2}\right)^2\right)^{\frac{1}{2}}$. The proposed explicit scheme is stable provided that $|Im(\lambda)| \le \frac{2}{\Delta t}$. Substitution of the equation $\frac{\partial \underline{V}}{\partial t} = \lambda\underline{V}$ into the equation $Ic\nabla \times \underline{V} = \lambda\underline{V}$ yields $\frac{1}{c}\frac{\partial \underline{V}}{\partial t} = I\nabla \times \underline{V}$ or $\nu\left(\frac{\partial V_z}{\partial y} - \frac{\partial V_y}{\partial z}\right) = \lambda V_x$, $\nu\left(\frac{\partial V_x}{\partial z} - \frac{\partial V_z}{\partial x}\right) = \lambda V_y$, and $\nu\left(\frac{\partial V_y}{\partial x} - \frac{\partial V_x}{\partial y}\right) = \lambda V_z$. These equations can be recast into the matrix equation $\underline{\underline{F}}\,\underline{V} = 0$. One can obtain the unique solution $\underline{V}$ from this matrix equation provided that the determinant of $\underline{\underline{F}}$ is equal to zero. Calculation of the solution from the quadratic polynomial equation $det\left(\underline{\underline{F}}\right) = 0$ leads to $\lambda^2 = -4c^2\left(\frac{F_x^2}{\Delta x^2} + \frac{F_y^2}{\Delta y^2}\right)$. To compute the solution of λ for all the possible wavenumbers k_x, k_y and k_z, we demand $Re(\lambda) = 0$ to obtain the stability condition $\Delta t \le \frac{1}{c}\left(\frac{\max(F_x^2)}{\Delta x^2} + \frac{\max(F_y^2)}{\Delta y^2} + \frac{\max(F_z^2)}{\Delta z^2}\right)^{-\frac{1}{2}}$. By substituting the previously derived coefficients a_1, a_2 and a_3 into this inequality equation, the stability condition, $\Delta t \le 0.673844\frac{h}{c}$, for the conditionally stable scheme proposed to solve the three dimensional Maxwell's equations is derived. For the sake of completeness, we have also derived the stability conditions for the one- and two-dimensional Maxwell's equations, which are $\Delta t \le 1.167132\frac{h}{c}$ and $\Delta t \le 0.825287\frac{h}{c}$, respectively.

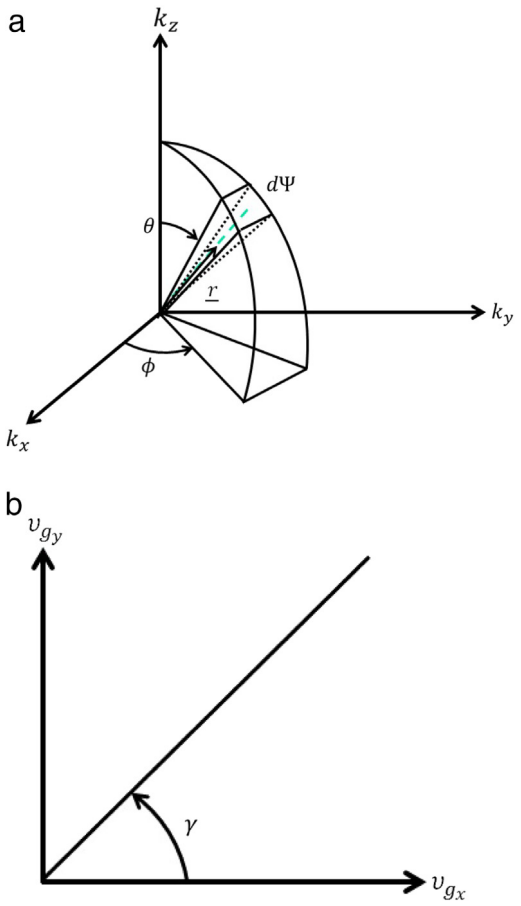

Fig. 1. (a) Schematic of a wave propagating along a direction defined by the zenith angle θ and the azimuthal angle ϕ. Note that $d\Psi$ $(= \sin\theta\, d\theta d\phi)$ denotes the differential solid angle for a wave along the direction $\underline{r}$; (b) Schematic of the group velocity angle γ at $k_z = 0$.

5.2. Anisotropy analysis

When simulating a multi-dimensional wave equation, it is essential to know how the predicted wave with its own numerical group/phase velocity traveling across the mesh depends on the magnitude and the direction of numerical angular frequency. To answer this question, it is customary to express the numerical/exact phase or group velocity vectors and the wavenumber vector in polar coordinates. In the present three dimensional analysis, two angles ϕ and θ shown schematically in Fig. 1(a) are used to express the wavenumber vector $\underline{k} = (k_x, k_y, k_z) = |k|(\sin\theta\ \cos\phi,\ \ \sin\theta\ \sin\phi,\ \ \cos\theta)$. In this spherical coordinate system, θ and ϕ are denoted respectively as the zenith and azimuthal angles. Given the definitions of these angles, the derived numerical dispersion relation equation can then be rewritten in terms of the polar coordinates as follows

$$\begin{aligned}\sin^2(\omega_{num}\Delta t/2) = {} & Cr_x^2\left(a_1\sin\left(\frac{5}{2}k\sin\theta\cos\phi\Delta x\right)+a_2\sin\left(\frac{3}{2}k\sin\theta\cos\phi\Delta x\right)+a_3\sin\left(\frac{1}{2}k\sin\theta\cos\phi\Delta x\right)\right)^2\\ & + Cr_y^2\left(a_1\sin\left(\frac{5}{2}k\sin\theta\sin\phi\Delta y\right)+a_2\sin\left(\frac{3}{2}k\sin\theta\sin\phi\Delta y\right)+a_3\sin\left(\frac{1}{2}k\sin\theta\sin\phi\Delta y\right)\right)^2\\ & + Cr_z^2\left(a_1\sin\left(\frac{5}{2}k\cos\theta\Delta z\right)+a_2\sin\left(\frac{3}{2}k\cos\theta\Delta z\right)+a_3\sin\left(\frac{1}{2}k\cos\theta\Delta z\right)\right)^2. \end{aligned} \tag{22}$$

According to the above equation, we know that the numerical angular frequency ω_{num} changes with the angle of wavenumber vector and the Courant numbers Cr_x $(\equiv \frac{c\Delta t}{\Delta x})$, Cr_y $(\equiv \frac{c\Delta t}{\Delta y})$ and Cr_z $(\equiv \frac{c\Delta t}{\Delta z})$.

In the anisotropy analysis, we set $\theta = \pi/2$ and then substitute it into the dispersion relation equation that accounts for the numerical angular frequency. The resulting equation turns out to be identical to the two-dimensional numerical dispersion relation equation derived in (x, y) coordinates. The exact and numerical angular frequencies are plotted with respect to k_x and k_y in Figs. 2(a) and 2(b), respectively, within the two-dimensional context for simplicity. In the plot

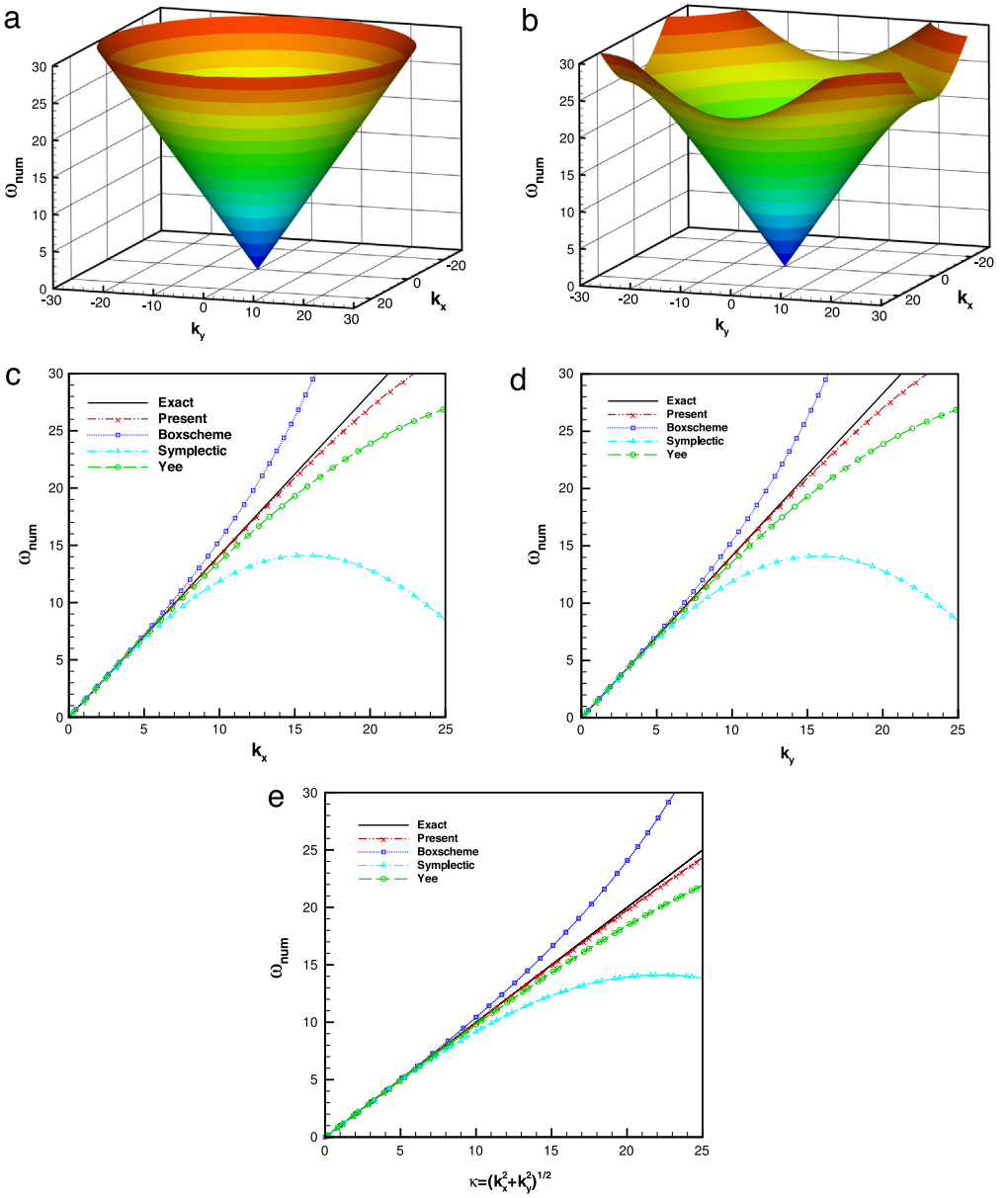

Fig. 2. The exact and the derived numerical angular frequencies in (a) and (b), respectively, are plotted with respect to k_x and k_y in $\underline{k} = (k_x, k_y)$ plane at $\Delta t = 0.01$, $\Delta x = \Delta y = 0.1$; (c) ω_{num} is plotted with respect to k_x for $k_y = 0$; (d) ω_{num} is plotted with respect to k_y for $k_x = 0$; (e) ω_{num} is plotted with respect to $|\underline{k}|$.

depicting the dispersion relation (Fig. 2(c)–(e)), the numerical dispersion surface ω_{num} is seen to be equal to that of the exact dispersion near the origin of $\underline{k} = (k_x, k_y) = |k|(\cos\phi, \sin\phi)$, where $\phi = \tan^{-1}\left(\frac{k_y}{k_x}\right)$. As the wavenumber is away from the origin of the (k_x, k_y) plane, the discrepancy between the numerical and exact angular frequencies illustrates the nonphysical parasitic waves in the numerical solutions [33]. For the sake of comparison, in Fig. 3 the numerical angular frequencies of the proposed scheme and the other three referenced schemes are plotted with respect to k_x and k_y. The error contours are also plotted in Fig. 4 for making a performance assessment on the current and the reference schemes.

We also derive the numerical group velocity optimized scheme from (22). The wave solution predicted from the proposed scheme with its numerical group velocity traveling across the grid system depends not only on the magnitude of the wavenumber vector $\underline{k}$, or $|\underline{k}|$, but also on the direction of the wavenumber vector $\underline{k}$, or $\tan^{-1}\left(\frac{k_y}{k_x}\right)$. Under the circumstances, the simulation error related to the derived grid-anisotropy [35] warrants a specific attention. Otherwise, the predicted wave may propagate at an erroneous speed and along a wrong direction. To gain a better understanding

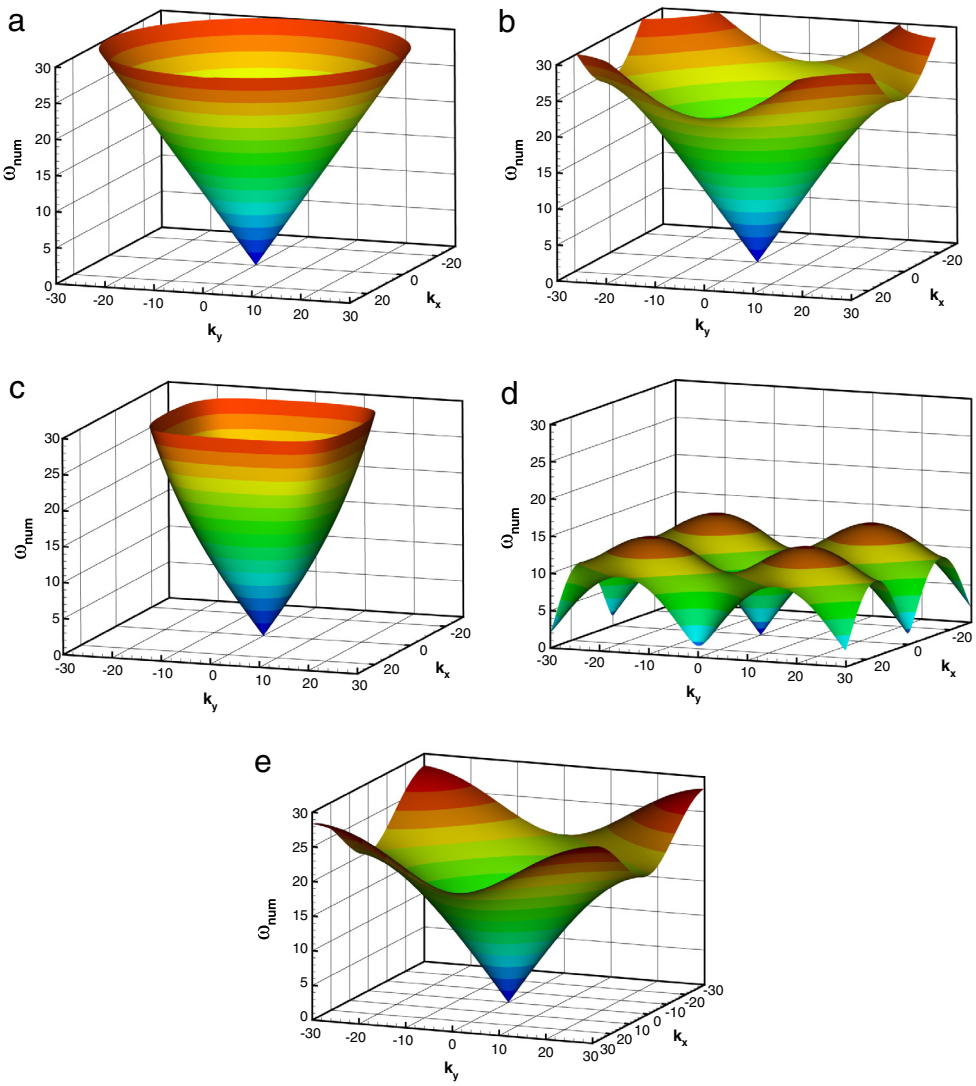

Fig. 3. Angular frequencies are plotted with respect to the wave numbers k_x and k_y for different schemes. (a) Exact; (b) optimized scheme; (c) box scheme [34]; (d) symplectic scheme [34]; (e) Yee's scheme [2].

of the anisotropy behavior, we consider, for example, a plane wave propagating along the direction with the unit vector $(\sin\theta' \cos\phi',\ \sin\theta' \sin\phi',\ \cos\theta')$ in the following error analysis.

Take a two-dimensional case as an example, the angle of group velocity vector can be expressed by the angle γ schematically shown in Fig. 1(b). The numerical group velocity can then be expressed by $\underline{\upsilon}_g \left(\equiv \frac{\partial \omega_{num}}{\partial \underline{k}}\right) = |\underline{\upsilon}_g|(\cos\gamma, \sin\gamma)$, where $\gamma = \tan^{-1}\left(\frac{(\upsilon_g)_y}{(\upsilon_g)_x}\right)$. The exact and numerical group velocity angles are then plotted with respect to the wavenumber angle. One can clearly find from the $\gamma - \phi$ plot in Fig. 5 that in the small modified wavenumber regime the predicted angle of group velocity agrees very well with the angle of exact wavenumber vector, which is $\frac{\pi}{4}$ shown in Fig. 3(a). When the value of kh increases, the resulting discrepancy between the exact, which is $\frac{\gamma}{\phi} = 1$, and the predicted ratios of $\frac{\gamma}{\phi}$ increases accordingly. This sheds light on the occurrence of dispersive error in higher wavenumber regime. The exact and numerical group velocity magnitudes are also plotted versus the wavenumber angle in Fig. 6. The contour values predicted at different Courant numbers for $\omega = 6$ are plotted as well in Fig. 7. For the sake of completeness, the contour values of the angular frequencies for $\omega = 6$, 12 and 16 are plotted in Fig. 8 for the proposed numerical phase velocity optimized scheme. One can see from this figure that the predicted and exact contours are essentially identical in case the magnitude of ω is less than 12. Based on the results tabulated in Table 2, we are confirmed to improve the solution accuracy using the proposed phase accurate scheme.

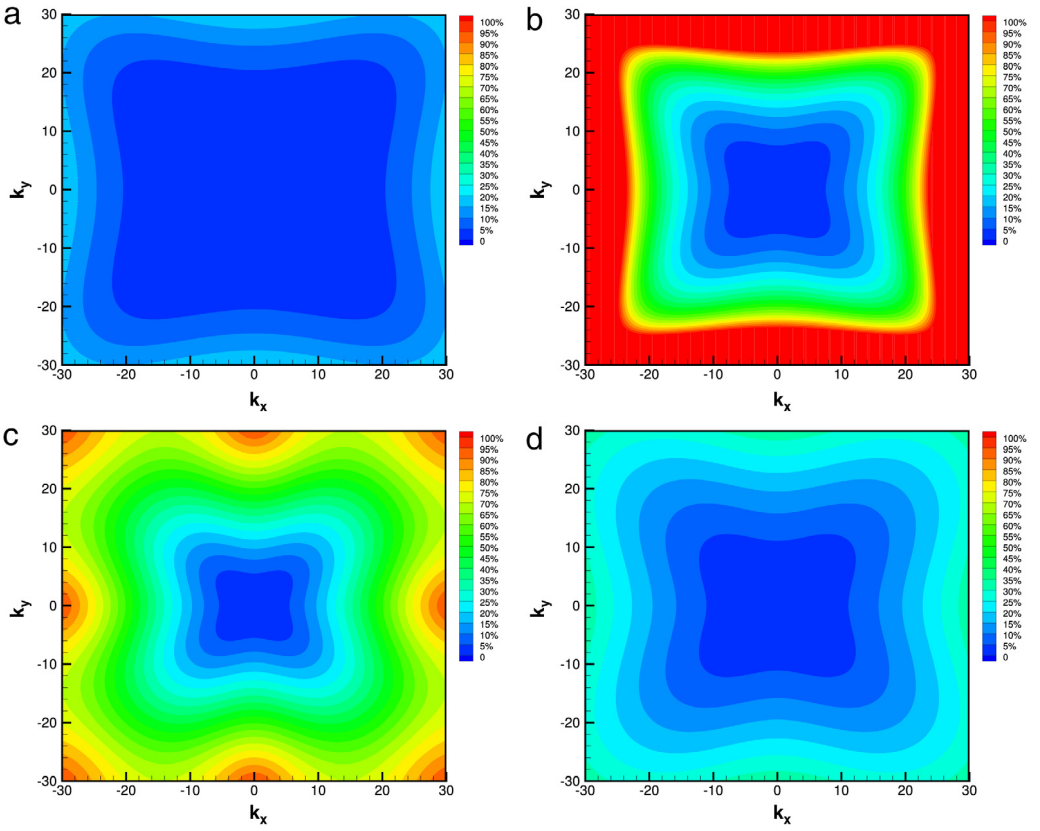

Fig. 4. The contour plots of $\frac{(\omega_{num}-\omega_{excat})}{\omega_{excat}} \times 100\%$ with respect to k_x and k_y for the present phase velocity optimized scheme and the reference schemes. (a) Present; (b) box scheme [34]; (c) symplectic scheme [34]; (d) Yee's scheme [2].

Table 2
The derived numerical dispersion relation equations and their spatial accuracy orders for the proposed and other three schemes. Schemes 1, 2, 3, 4 denote respectively the current, box [34], symplectic [34], and Yee [2] schemes. Note that the exact dispersion relation equation is $\frac{\omega^2}{c^2} = k_x^2 + k_y^2$.

Scheme	Numerical dispersion relation equation	Spatial accuracy order
1	$\frac{\omega^2}{4c^2}\left(\frac{\sin(\omega\Delta t/2)}{\omega\Delta t}\right)^2 = k_x^2\left(\frac{5}{2}a_1\frac{\sin(\frac{5}{2}k_x\Delta x)}{\frac{5}{2}k_x\Delta x} + \frac{3}{2}a_2\frac{\sin(\frac{3}{2}k_x\Delta x)}{\frac{3}{2}k_x\Delta x} + \frac{1}{2}a_3\frac{\sin(\frac{1}{2}k_x\Delta x)}{\frac{1}{2}k_x\Delta x}\right)^2$ $+k_y^2\left(\frac{5}{2}a_1\frac{\sin(\frac{5}{2}k_y\Delta y)}{\frac{5}{2}k_y\Delta y} + \frac{3}{2}a_2\frac{\sin(\frac{3}{2}k_y\Delta y)}{\frac{3}{2}k_y\Delta y} + \frac{1}{2}a_3\frac{\sin(\frac{1}{2}k_y\Delta y)}{\frac{1}{2}k_y\Delta y}\right)^2$ $+k_z^2\left(\frac{5}{2}a_1\frac{\sin(\frac{5}{2}k_z\Delta z)}{\frac{5}{2}k_z\Delta z} + \frac{3}{2}a_2\frac{\sin(\frac{3}{2}k_z\Delta z)}{\frac{3}{2}k_z\Delta z} + \frac{1}{2}a_3\frac{\sin(\frac{1}{2}k_z\Delta z)}{\frac{1}{2}k_z\Delta z}\right)^2$	4
2	$\frac{\tan^2(\frac{1}{2}\omega\Delta t)}{c^2\Delta t^2} = \frac{\tan^2(\frac{1}{2}k_x\Delta x)}{\Delta x^2} + \frac{\tan^2(\frac{1}{2}k_y\Delta y)}{\Delta y^2}$	2
3	$4\frac{\tan^2(\frac{1}{2}\omega\Delta t)}{c^2\Delta t^2} = \frac{\sin^2(k_x\Delta x)}{\Delta x^2} + \frac{\sin^2(k_y\Delta y)}{\Delta y^2}$	2
4	$\frac{\sin^2(\frac{1}{2}\omega\Delta t)}{c^2\Delta t^2} = \frac{\sin^2(\frac{1}{2}k_x\Delta x)}{\Delta x^2} + \frac{\sin^2(\frac{1}{2}k_y\Delta y)}{\Delta y^2}$	2

In Table 3, the first and second leading error terms in the modified equation, $\frac{\partial E_z}{\partial t} = \frac{1}{\varepsilon}\left(\frac{\partial H_y}{\partial x} - \frac{\partial H_x}{\partial y}\right) + \frac{A}{\varepsilon}\frac{\partial^5 H_y}{\partial x^5}dx^4 + \frac{B}{\varepsilon}\frac{\partial^7 H_y}{\partial x^7 dx^6} + \cdots$ are tabulated for the proposed and referenced schemes are summarized at different Courant numbers. One can confirm for one more time that the formal accuracy has been increased using the currently proposed scheme.

For taking into account all the possible *EM* wave propagation directions, the error between the numerical and exact phase velocities, defined as $1 - \frac{|\underline{u}_p(\omega,\theta',\phi')|}{c_0=(\mu\varepsilon)^{1/2}}$, is worthy to be calculated in the three dimensional context. Towards this perspective, this error is calculated in the spherical coordinate system by integrating the phase velocity error over a differential area $r^2\sin\theta' d\theta' d\phi'$. Note that the wave is defined within $0 \le \theta' \le 2\pi$ and $0 \le \phi' \le \pi$ and is in association with a differential solid angle $\sin\theta' d\theta' d\phi'$ shown schematically in Fig. 1(a). The resulting error per the spherical area $4\pi r^2$ can be computed

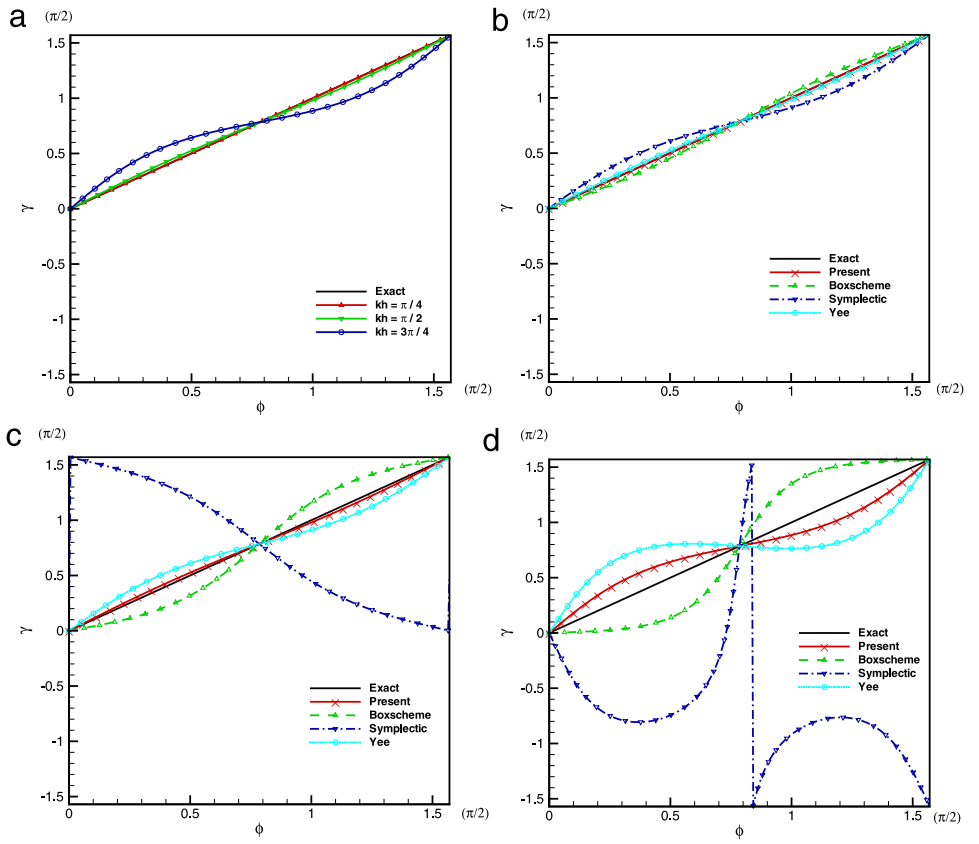

Fig. 5. The exact and numerical group velocity angles γ are plotted with respect to the wavenumber angle ϕ at different modified wavenumbers. (a) Optimized scheme; (b) comparison of different schemes at $kh = \frac{\pi}{4}$; (c) comparison of different schemes at $kh = \frac{\pi}{2}$; (d) comparison of different schemes at $kh = \frac{3\pi}{4}$.

Table 3
The coefficients A and B for the first and second leading error terms shown, respectively, in the modified equation and their values at different Cr numbers are tabulated. (a) The expressions of A and B for different schemes; (b) the values of A and B at different values of Cr obtained for different schemes.

(a)

	A	B
Present	$\frac{625}{384}a_1 + \frac{81}{640}a_2 + \frac{1}{1920}a_3 - \frac{Cr^4}{576} - \frac{Cr^4}{1920}$	$\frac{15625}{64512}a_1 + \frac{243}{35840}a_2 + \frac{1}{322560}a_3$ $-\frac{Cr^4}{24}(\frac{625}{384}a_1 + \frac{81}{640}a_2 + \frac{1}{1920}a_3) - \frac{Cr^6}{40320}$
Box	$\frac{1}{6}h^2(Cr^2 - 1)$	$\frac{1}{6}h^2Cr^2$
Symplectic	$\frac{1}{6}h^2(Cr^2 + 2)$	$\frac{1}{6}h^2Cr^2$
Yee	$\frac{1}{24}h^2(Cr^2 + 1)$	$\frac{1}{1920}h^4(Cr^4 + 1)$

(b)

		Present	Box	Symplectic	Yee
$Cr = 0.1$	A	−0.00075689	−0.165	0.335	0.04208333
	B	0.00053188	0.00166667	0.00166667	0.00052089
$Cr = 0.2$	A	−0.00478130	−0.16	0.34	0.04333333
	B	−0.00032961	0.00666667	0.00666667	0.00052167
$Cr = 0.4$	A	−0.02095548	−0.4	0.36	0.04833333
	B	−0.00376243	0.0266666	0.02666667	0.00053417
$Cr = 0.6$	A	−0.04819898	−0.085	0.415	0.05666667
	B	−0.00931450	0.06	0.06	0.00058833

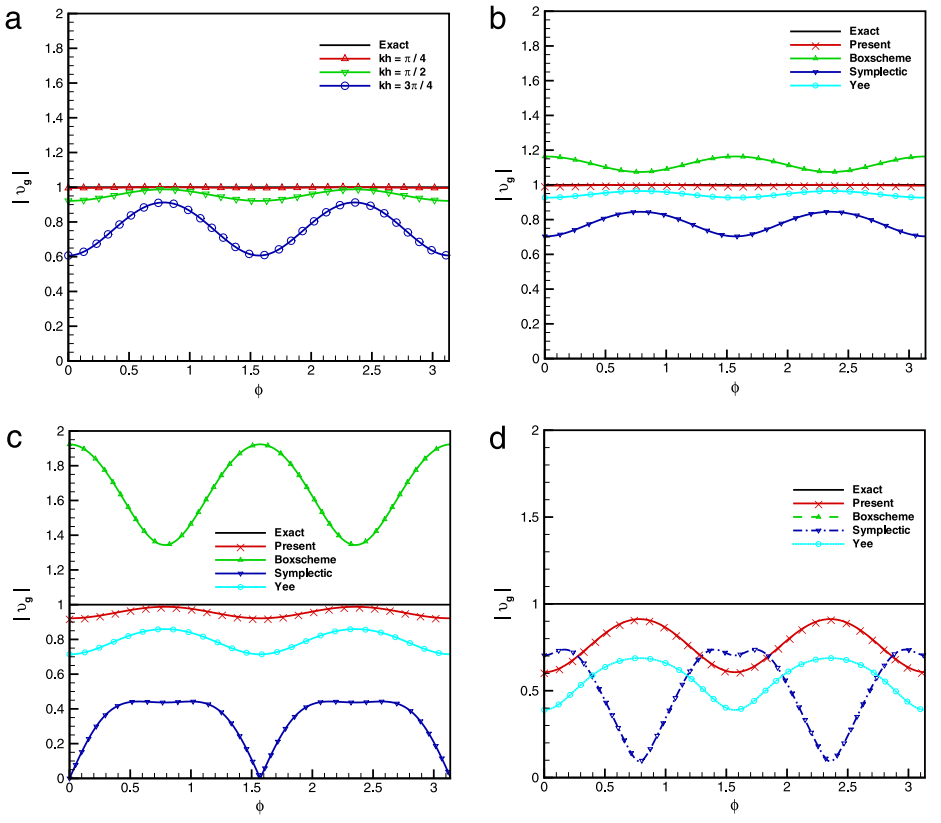

Fig. 6. The exact and numerical group velocity magnitudes are plotted with respect to the wavenumber angle ϕ at different modified wavenumbers. (a) Optimized scheme; (b) comparison of the numerical group velocities for different schemes at $kh = \frac{\pi}{4}$; (c) comparison of the numerical group velocities for different schemes at $kh = \frac{\pi}{2}$; (d) comparison of the numerical group velocities for different schemes at $kh = \frac{3\pi}{4}$.

according to the definition given below

$$E_{3D}(\omega) = \frac{1}{4\pi}\int_0^{\pi}\int_0^{2\pi} 1 - \frac{|\underline{u}_p(\omega,\theta',\phi')|}{(\mu\varepsilon)^{1/2}}\sin\theta' d\theta' d\phi'. \tag{23}$$

The errors plotted accordingly are tabulated in Fig. 9.

5.3. Dispersion analysis

Now, in Fig. 10 we plot the derived coefficients a_1, a_2 and a_3 with respect to the wavenumber angle $\phi \equiv \tan^{-1}\left(\frac{k_y}{k_x}\right)$. The weighting coefficients a_1, a_2 and a_3 obtained at each point in the domain can then be interpolated through the data tabulated in Table 4 or plotted in Fig. 10. Depending on the magnitude of speed of light, the referenced characteristic speeds $c\ \sin\gamma$ and $c\ \cos\gamma$, where γ denotes the angle of phase velocity vector, differ in the physical domain on a pointwise basis. At each spatial location we can then calculate its local Courant numbers Cr_x and Cr_y and hence obtain the corresponding set of the interpolated weighting coefficients from the coefficients a_1 to a_3, which are plotted in Fig. 11.

Given the definition of $k^2 = k_x^2 + k_y^2$, the wavenumber components can be expressed as $k_x = k\ \cos\phi$ and $k_y = k\ \sin\phi$. For the sake of comparison and discussion of the computed results, two extra parameters are defined. The first one, which is $N_\lambda = \frac{\lambda}{h}$, denotes the number of points per wavelength λ $(=\frac{2\pi}{k})$. The other parameter is the CFL number $Cr = \frac{c\Delta t}{h}$. The speed of light c is chosen as the referenced speed and $h = \Delta x = \Delta y$ is the uniform grid spacing. Given these definitions, the numerical phase velocity $\underline{\upsilon}_p$, which is defined as the ratio of the numerical angular frequency and the wavenumber $\underline{k}$, can be derived. We can express $e^{I\omega_{num}\Delta t}$ by virtue of Eq. (19) to get $e^{I\omega\Delta t} = e^{I\Delta t(\omega_R + I\omega_I)} = e^{-\omega_I\Delta t}(\cos(\omega_R\Delta t) + I\sin(\omega_R\Delta t))$. Define $\hat{R} = e^{-\omega_I\Delta t}\cos(\omega_R\Delta t)$ and $\hat{I} = e^{-\omega_I\Delta t}\sin(\omega_R\Delta t)$, the value of $\tan(\omega_R\Delta t) = \frac{\hat{I}}{\hat{R}}$ and, then, the ratio of the numerical phase velocity $|\underline{\upsilon}_p| = |\frac{\omega_R}{\underline{k}}|$ versus the exact phase velocity c can be calculated from the following equation [36]

$$\frac{\upsilon_p}{c} = \frac{\omega_R}{ck} = \frac{N_\lambda}{2\pi Cr}\tan^{-1}\left(\frac{\hat{I}}{\hat{R}}\right). \tag{24}$$

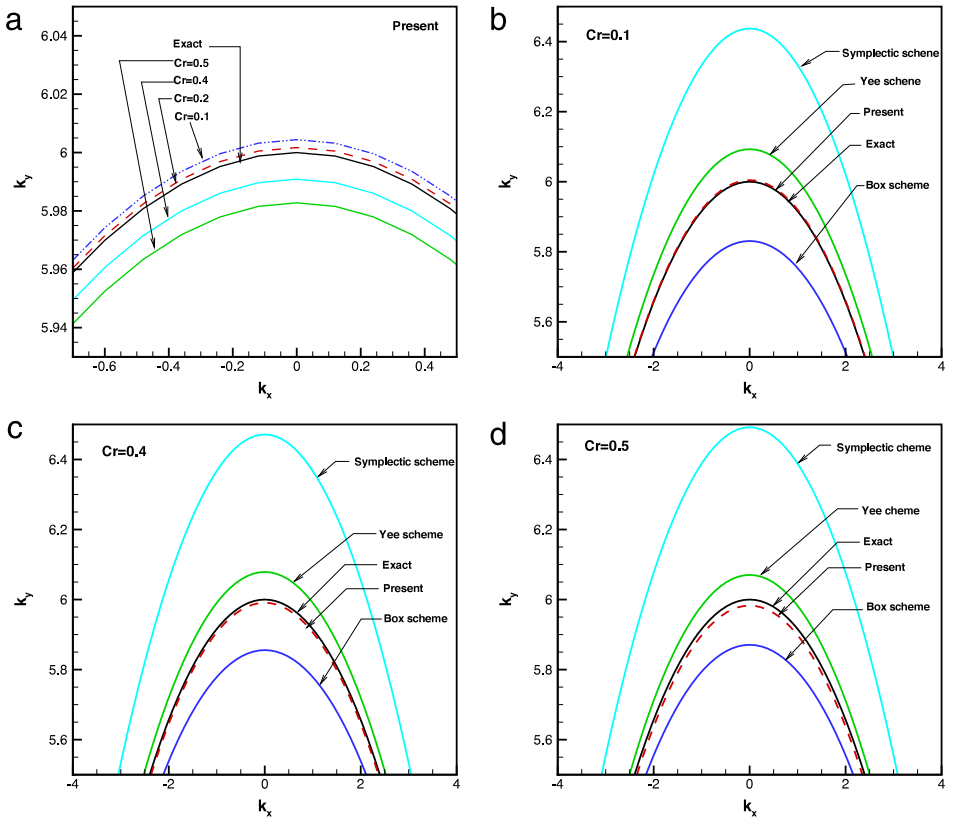

Fig. 7. The contours of $\omega_{num} = 6$ are plotted with respect to k_x and k_y at different Courant numbers for different schemes. (a) $Cr = 0.1, 0.2, 0.4, 0.5$; (b) $Cr = 0.1$; (c) $Cr = 0.4$; (d) $Cr = 0.5$.

In the current comparison study, the ratios of the derived numerical phase velocity and the exact phase velocity, which is $\frac{\upsilon_p}{c}$, are plotted in Fig. 12 for the Box scheme, symplectic scheme, and Yee's scheme at different values of N_λ. For the case of fewer grid points per wavelength, our scheme is clearly seen to have a better phase velocity. Also, the proposed dispersion-error reducing scheme performs better near the angle $\phi = 45°$. When increasing the value of N_λ, the numerical phase velocity approaches the exact phase velocity asymptotically. In addition, one can clearly know from Fig. 4 that the present scheme has a better agreement between its numerical and exact dispersion relation equations.

6. Absorbing boundary condition

Numerical simulation of wave propagation in open domains requires the truncation of the physical domain under investigation. Otherwise, in many cases it is difficult for us to get an adequate computational resource to carry out calculations on large sized problems. Implementation of a proper set of artificial boundary conditions on the truncated boundaries is therefore needed to prevent unphysical wave reflection that may contaminate the predicted solution.

One can directly prescribe a physical boundary condition to suppress the reflected wave [37]. Implementation of this comparatively accurate boundary condition suffers some problems mentioned in [38]. The other alternative to prevent wave reflection from the truncated boundary underlies the concept of splitting the domain into the Perfectly Matched Layer (PML) and the non-PML zones. The PML approach of Berenger [9] can be applied to effectively absorb outgoing waves from the interior of computational domain without reflecting them back to the interior. A specially tailored absorbing layer surrounding the finite physical region should have the perfectly matched absorbing property in the sense that any wave propagating in the domain of interest does not produce any unphysical reflection wave when it is incident upon the interface separating the PML and non-PML regions. The underlying strategy is to properly define the material parameters in the absorbing layer so as to render a perfect match on the impedances of the media in the physical region and the boundary layer. After the pioneering work of the split field PML formulation, the Uniaxial PML (UPML) method of Gedney [39] and the Convolutional PML (CPML) method of Roden and Gedney [40] have been developed with great success to simulate *EM* wave.

Within the framework of PML, to get a spatial damping effect either a wave vector or a position vector is transformed to a complex-valued vector. One can implement PML, for example, in terms of the complex stretching physical coordinate axis [10]. Through the mapping from a real position vector to a complex space, one can rewrite the Maxwell's equations in

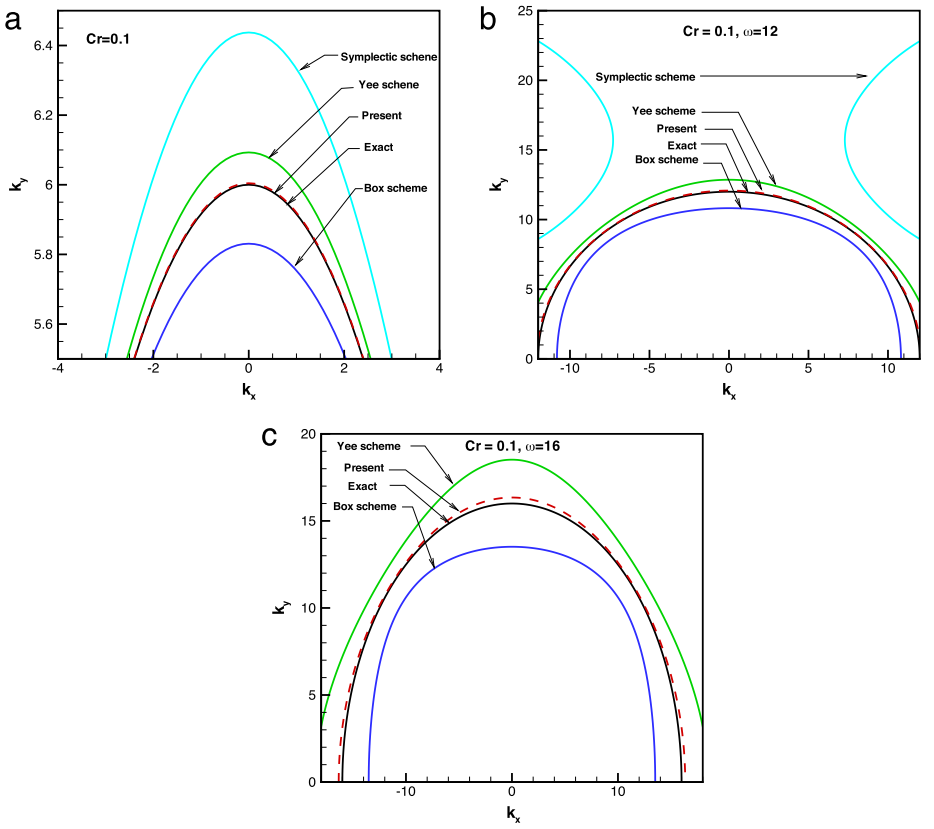

Fig. 8. Plot of the exact and numerical angular frequencies with respect to k_x and k_y at different angular frequencies for the case investigated at $Cr = 0.1$. (a) $\omega = 6$; (b) $\omega = 12$; (c) $\omega = 16$.

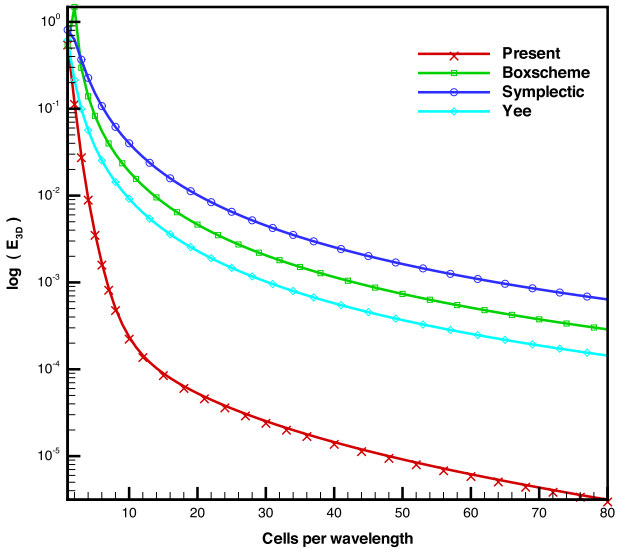

Fig. 9. Plot of the values of E_{3D} with respect to the number of cells per wavelength N_λ using the numerical phase velocity optimized scheme and the three other schemes.

stretched coordinates which are the functions of the complex stretching factor detailed in [38]. Three real-valued parameters σ_i $(i = x, y, z)$ expressed in stretching factors $s_i = 1 + \frac{\sigma_i}{I\omega\varepsilon_0}$ along the x, y, z directions need to be tuned for rendering an optimum performance, where I denotes the imaginary unit. Another novel implementation of CFS-PML [12] is referred to as the convolutional PML (CPML) [40]. CPML, implemented on the stretched coordinates as well, is featured with the

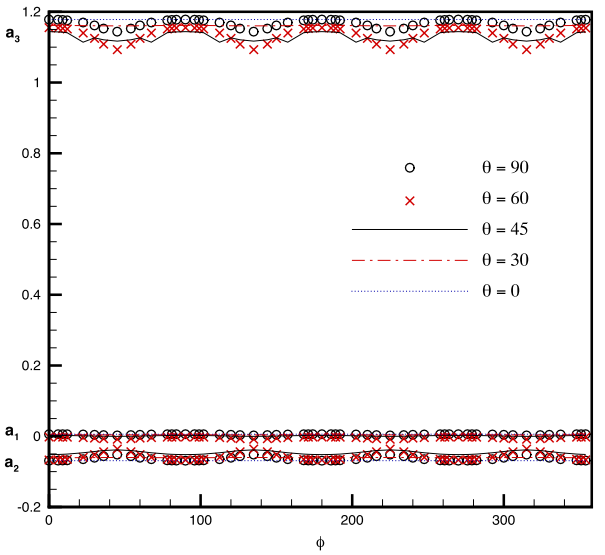

Fig. 10. The derived weighting coefficients a_1, a_2 and a_3 are plotted with respect to the wave propagation angle $\phi \equiv \tan^{-1}(\frac{k_y}{k_x})$ at different zenith angles θ at $Cr = (Cr_x^2 + Cr_y^2 + Cr_z^2)^{1/2} = 0.2$.

Table 4
The derived coefficients a_1, a_2 and a_3 shown in (15) for the proposed three dimensional scheme. Note that $\sin(\frac{\pi}{2} - \phi) = \cos\phi, \cos(\frac{\pi}{2} - \phi) = \sin\phi, \sin(\frac{3\pi}{2} - \phi) = -\cos\phi, \cos(\frac{3\pi}{2} - \phi) = \sin\phi, \sin(\pi - \phi) = \sin\phi, \cos(\pi - \phi) = -\cos\phi, \sin(-\phi) = -\sin\phi, \cos(-\phi) = \cos\phi$.

	$\theta = 0^\circ, 180^\circ$	$\theta = 30^\circ, 150^\circ$	$\theta = 45^\circ, 135^\circ$	$\theta = 60^\circ, 120^\circ$	$\theta = 90^\circ$
$\phi = 0^\circ, 90^\circ$ $= 180^\circ, 270^\circ$	$a_1 = 0.005810$ $a_2 = -0.069054$ $a_3 = 1.178108$	$a_1 = 0.004149$ $a_2 = -0.060746$ $a_3 = 1.161493$	$a_1 = 0.002385$ $a_2 = -0.051924$ $a_3 = 1.143849$	$a_1 = 0.004149$ $a_2 = -0.060746$ $a_3 = 1.161493$	$a_1 = 0.005811$ $a_2 = -0.069054$ $a_3 = 1.178108$
$\phi = 6^\circ, 84^\circ, 96^\circ, 174^\circ$ $= 186^\circ, 264^\circ$ $= 276^\circ, 354^\circ$	$a_1 = 0.005781$ $a_2 = -0.068790$ $a_3 = 1.177581$	$a_1 = 0.004059$ $a_2 = -0.060291$ $a_3 = 1.160582$	$a_1 = 0.002309$ $a_2 = -0.051547$ $a_3 = 1.1430945$	$a_1 = 0.004144$ $a_2 = -0.060719$ $a_3 = 1.161437$	$a_1 = 0.005811$ $a_2 = -0.069054$ $a_3 = 1.178108$
$\phi = 9^\circ, 81^\circ, 99^\circ, 171^\circ$ $= 189^\circ, 261^\circ$ $= 279^\circ, 351^\circ$	$a_1 = 0.005691$ $a_2 = -0.068454$ $a_3 = 1.176909$	$a_1 = 0.003941$ $a_2 = -0.059701$ $a_3 = 1.159411$	$a_1 = 0.002215$ $a_2 = -0.051076$ $a_3 = 1.142151$	$a_1 = 0.004137$ $a_2 = -0.060684$ $a_3 = 1.16137$	$a_1 = 0.005811$ $a_2 = -0.069054$ $a_3 = 1.178108$
$\phi = 12^\circ, 78^\circ, 102^\circ, 168^\circ$ $= 192^\circ, 258^\circ$ $= 282^\circ, 348^\circ$	$a_1 = 0.005594$ $a_2 = -0.067971$ $a_3 = 1.175942$	$a_1 = 0.003771$ $a_2 = -0.058855$ $a_3 = 1.15771$	$a_1 = 0.002083$ $a_2 = -0.050416$ $a_3 = 1.140832$	$a_1 = 0.004128$ $a_2 = -0.060640$ $a_3 = 1.161279$	$a_1 = 0.005811$ $a_2 = -0.069054$ $a_3 = 1.178108$
$\phi = 22.5^\circ, 67.5^\circ, 112.5^\circ$ $= 157.5^\circ, 202.5^\circ, 247.5^\circ$ $= 292.5^\circ, 337.5^\circ$	$a_1 = 0.004970$ $a_2 = -0.064850$ $a_3 = 1.169700$	$a_1 = 0.002639$ $a_2 = -0.053195$ $a_3 = 1.146390$	$a_1 = 0.001342$ $a_2 = -0.046708$ $a_3 = 1.133415$	$a_1 = 0.004084$ $a_2 = -0.060422$ $a_3 = 1.1608433$	$a_1 = 0.005811$ $a_2 = -0.069054$ $a_3 = 1.178108$
$\phi = 30^\circ, 60^\circ, 120^\circ, 150^\circ$ $= 210^\circ, 240^\circ$ $= 300^\circ, 330^\circ$	$a_1 = 0.004149$ $a_2 = -0.060746$ $a_3 = 1.161493$	$a_1 = 0.001121$ $a_2 = -0.045605$ $a_3 = 1.131211$	$a_1 = 0.0006261$ $a_2 = -0.043131$ $a_3 = 1.126261$	$a_1 = 0.004051$ $a_2 = -0.060257$ $a_3 = 1.160513$	$a_1 = 0.005811$ $a_2 = -0.069054$ $a_3 = 1.178108$
$\phi = 36^\circ, 54^\circ, 126^\circ, 144^\circ$ $= 216^\circ, 234^\circ$ $= 306^\circ, 324^\circ$	$a_1 = 0.003262$ $a_2 = -0.056308$ $a_3 = 1.152616$	$a_1 = -0.000503$ $a_2 = -0.037483$ $a_3 = 1.114966$	$a_1 = 0.000085$ $a_2 = -0.040426$ $a_3 = 1.120852$	$a_1 = 0.004031$ $a_2 = -0.060154$ $a_3 = 1.160307$	$a_1 = 0.005811$ $a_2 = -0.069054$ $a_3 = 1.178108$
$\phi = 45^\circ, 135^\circ$ $= 225^\circ, 315^\circ$	$a_1 = 0.002385$ $a_2 = -0.051925$ $a_3 = 1.143849$	$a_1 = -0.002069$ $a_2 = -0.029658$ $a_3 = 1.099315$	$a_1 = -0.000299$ $a_2 = -0.038507$ $a_3 = 1.117015$	$a_1 = 0.004018$ $a_2 = -0.06009$ $a_3 = 1.16018$	$a_1 = 0.005811$ $a_2 = -0.069054$ $a_3 = 1.178108$

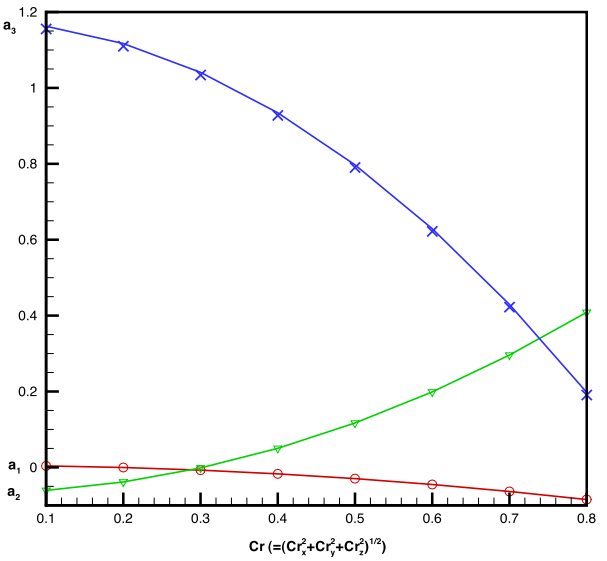

Fig. 11. The derived coefficients a_1, a_2 and a_3 are plotted with respect to the Courant numbers $Cr = (Cr_x^2 + Cr_y^2 + Cr_z^2)^{1/2}$ using the numerical phase velocity optimized scheme at $\theta = \phi = \frac{\pi}{4}$.

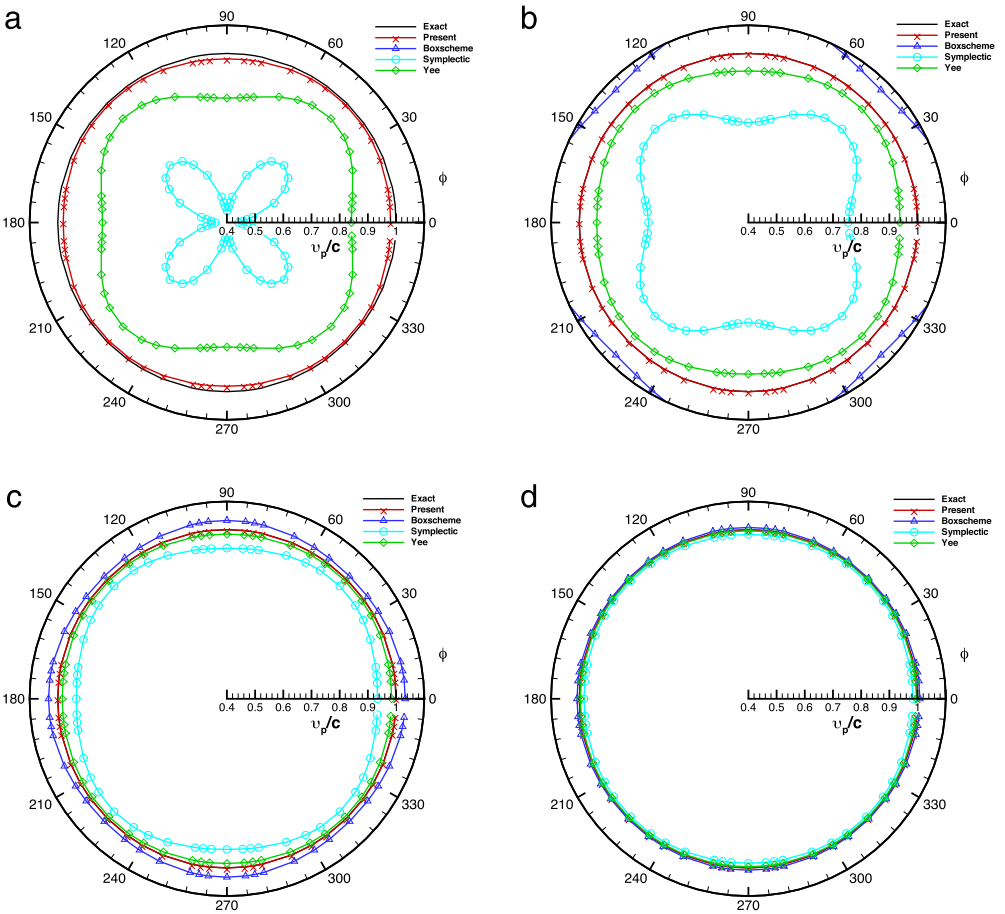

Fig. 12. Comparison of the phase velocity ratios $\frac{V_p}{c}$ versus θ at different values of N_λ. (a) $N_\lambda = 3.1$; (b) $N_\lambda = 5$; (c) $N_\lambda = 10$; (d) $N_\lambda = 20$.

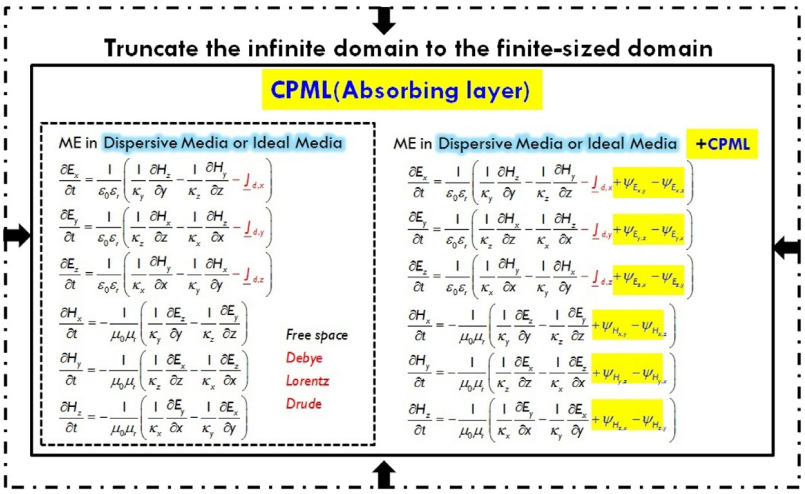

Fig. 13. The *EM* equations in the domain surrounded by the attached convolutional perfectly matched layer.

Table 5
The predicted L_2-*error norms* obtained at $T = 5$(s) and the *CPU* time.

Present			Yee [2]		
L_2-error norm	Grid	CPU time (s)	L_2-error norm	Grid	CPU time (s)
7.0023E−02	51 × 51	0.8580	7.0534E−03	198 × 198	3.2760
4.3059E−03	61 × 61	1.4352	4.3346E−03	254 × 254	6.8640
2.3572E−03	71 × 71	2.2620	2.3627E−03	346 × 346	17.5813

introduction of a recursive convolution and a complex frequency shifted parameter. CPML schematically shown in Fig. 13 has a number of advantages over the traditional implementation of the UPML. The stretching factor $s_i (i = x, y, z)$ is expressed as $s_i = k_i + \frac{\sigma_i}{\alpha_i + I\omega\varepsilon_0}$, where $k_i \geq 1$ is a real.

7. Verification studies of ideal Maxwell's equations

The explicit symplectic PRK scheme with the optimized numerical dispersion relation equation developed in staggered grids will be verified firstly by solving the TM-mode Maxwell's equations at $\mu = 1$ and $\varepsilon = 1$ in $-1 \leq x \leq 1$, $-1 \leq y \leq 1$ and $-1 \leq z \leq 1$, In this study the problem amenable to the analytic solution given below will be solved subject to the initial solenoidal solutions $E_z(x, y, 0) = \sin(3\pi x)\sin(4\pi y)$, $H_x(x, y, 0) = -\frac{4}{5}\cos(3\pi x)\cos(4\pi y)$ and $H_y(x, y, 0) = -\frac{3}{5}\cos(3\pi x)\cos(4\pi y)$

$$\begin{aligned} E_z(x, y, t) &= \sin(3\pi x - 5\pi t)\sin(4\pi y), \\ H_x(x, y, t) &= -\frac{4}{5}\cos(3\pi x - 5\pi t)\cos(4\pi y), \\ H_y(x, y, t) &= -\frac{3}{5}\cos(3\pi x - 5\pi t)\cos(4\pi y). \end{aligned} \tag{25}$$

According to the computed errors tabulated in Table 5 and the spatial rate of convergence in Fig. 14, the proposed dual-preserving scheme in free space for the TM-mode Maxwell's equations is analytically verified. It is noted that the predicted numerical spatial rate of convergence is 3.14. The reason leading to the determinated numerical rate of convergence is that at the end points and the points next to end points we apply the one-sided second-order accurate scheme rather than the fourth-order accurate scheme applied at interior points.

The predicted and exact energy densities given in (10) are plotted against time in Fig. 15. Note that the Hamiltonian defined in (9) is trivially equal to zero in any two-dimensional TM-mode Maxwell's equations. The value of $\nabla \cdot \underline{H}$ is predicted to be almost equal to zero in Fig. 16, indicating that the Gauss's law is satisfied discretely using the explicit symplectic partitioned Runge–Kutta scheme.

The Maxwell's equations amenable to the second set of exact solutions are then solved in $-\pi \leq x \leq \pi$, $-\pi \leq y \leq \pi$ and $-\pi \leq z \leq \pi$, and the solution of Maxwell's equations is sought at $\mu = 1$ and $\varepsilon = 1$. Subject to the initial solenoidal solutions $E_x(x, y, z, 0) = E_y(x, y, z, 0) = E_z(x, y, z, 0) = 0, H_x(x, y, z, 0) = \cos(x+y+z), H_y(x, y, z, 0) = \frac{1}{2}(-1+\sqrt{3})\cos(x+y+z)$

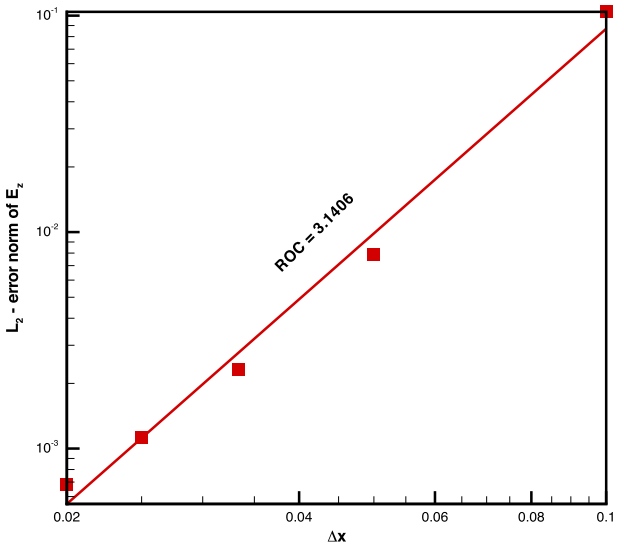

Fig. 14. Plot of the errors with respect to grid spacings for showing the predicted numerical rate of convergence.

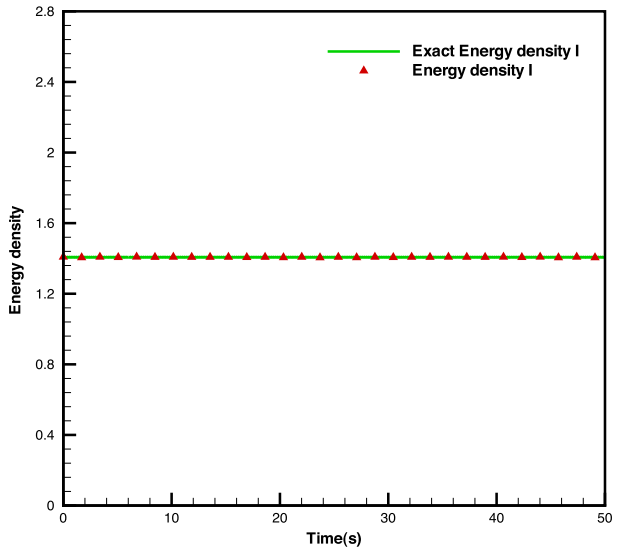

Fig. 15. Comparison of the computed and exact energy densities with respect to time for the first exact problem using the currently developed scheme.

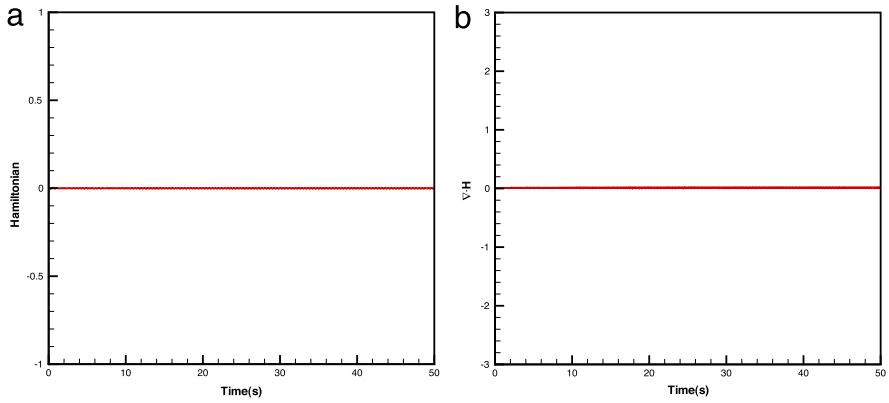

Fig. 16. Plot of Hamiltonian function and $\nabla \cdot \underline{H}$ with respect to time. (a) Hamiltonian function; (b) $\nabla \cdot \underline{H}$.

Table 6
The computed L_2-*error norms* and the *CPU* time at $T = 5$(s).

	L_2-error norm		CPU time (s)	
	Present	Yee [2]	Present	Yee [2]
$51 \times 51 \times 51$	1.1311E−04	6.9636E−04	7.4880	3.5568
$61 \times 61 \times 61$	8.0305E−05	4.8682E−04	14.4144	7.3476
$71 \times 71 \times 71$	5.9525E−05	3.5937E−04	23.9305	13.6657
$81 \times 81 \times 81$	4.5102E−05	2.7428E−04	38.8598	23.0569

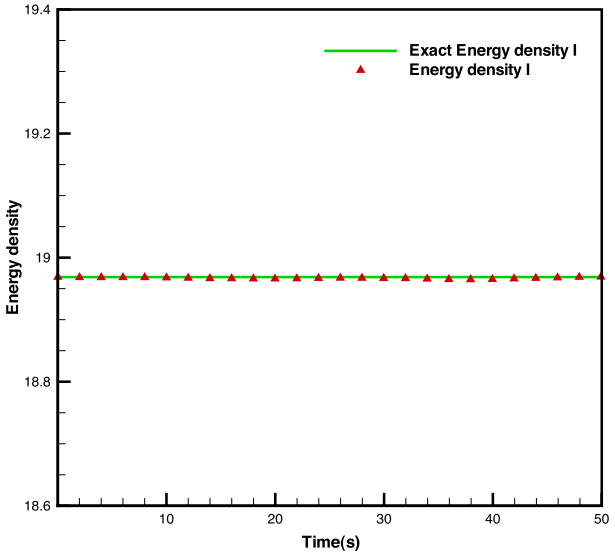

Fig. 17. Comparison of the computed and exact energy densities with respect to time using the currently developed scheme.

and $H_z(x, y, z, 0) = -\frac{1}{2}(1+\sqrt{3})\cos(x+y+z)$, the exact electric and magnetic field solutions to Eqs. (7)–(8) are as follows

$$\begin{aligned}
E_x(x, y, z, t) &= \sin(\sqrt{3}t)\sin(x+y+z),\\
E_y(x, y, z, t) &= -\frac{1}{2}(1+\sqrt{3})\sin(\sqrt{3}t)\sin(x+y+z),\\
E_z(x, y, z, t) &= \frac{1}{2}(-1+\sqrt{3})\sin(\sqrt{3}t)\sin(x+y+z),\\
H_x(x, y, z, t) &= \cos(\sqrt{3}t)\cos(x+y+z),\\
H_y(x, y, z, t) &= \frac{1}{2}(-1+\sqrt{3})\cos(\sqrt{3}t)\cos(x+y+z),\\
H_z(x, y, z, t) &= -\frac{1}{2}(1+\sqrt{3})\cos(\sqrt{3}t)\cos(x+y+z).
\end{aligned} \tag{26}$$

According to the computed errors of Yee's scheme tabulated in Table 6, the predicted and exact energy densities plotted against time in Fig. 17 and the Hamiltonian plotted in Fig. 18, the proposed dual-preserving scheme in free space for the Maxwell's equations is again analytically verified. Besides performing the verification study, the Hamiltonian in (9) and the energy density given in (10) are calculated as well.

7.1. Mie scattering problem

Two Mie scattering problems are then investigated in a cube with the cross-section area of 760×760 nm^2 or in -380 nm $\le x, y, z \le 380$ nm using the scheme being numerically verified. The diameter of the dielectric cylinder under current study is 126.56 nm and it is located at the center of a cube with the volume of 720^3 nm^3. The value of ε_r of this isotropic cylinder in homogeneous air medium is 12.1104. The incident x-polarized plane wave with the amplitude of 0.5 $\frac{v}{m}$ and the angular frequency of 13.263 $\frac{\text{rad}}{s}$ propagates along the positive x-direction according to the one-dimensional Maxwell's equations $\frac{\partial E_z}{\partial t} = \frac{1}{\varepsilon}\nabla \times H$, $\frac{\partial H}{\partial t} = -\frac{1}{\mu}\nabla \times \underline{E}$. The physical domain has been divided into two distinct regions, namely, the total field containing the investigated dielectric cylinder and the scattered field enclosing the three-dimensional total

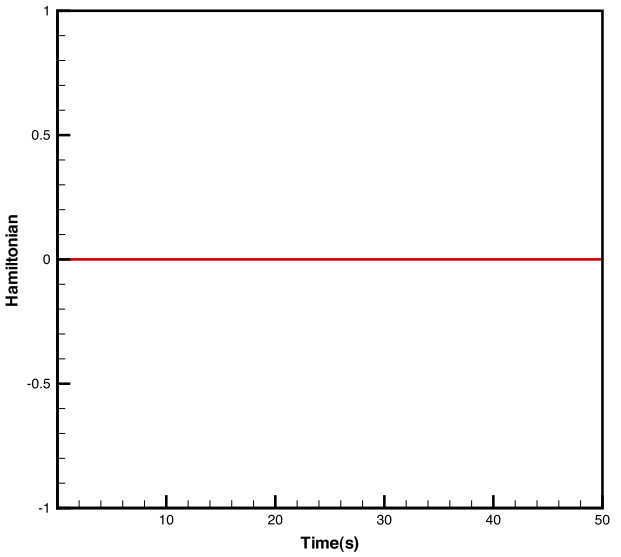

Fig. 18. Plot of Hamiltonian function with respect to time.

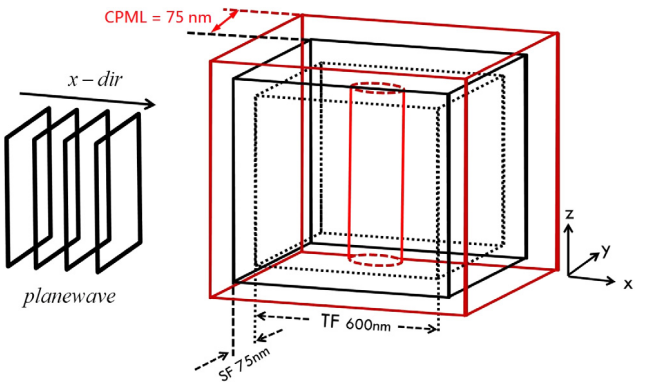

Fig. 19. Schematic of the 3D Mie scattering problem.

field. The scattered field components are stored only in the scattered field. To simulate the scattered wave from the dielectric cylinder in free space, the CPML absorbing boundary condition is adopted.

The first problem under investigation solves the *EM* wave scattered from a cylindrically-shaped scatter located at the center of the physical domain schematically shown in Fig. 19. All the results are calculated at the same Courant number $Cr = 0.2$, which corresponds to the specified time increment $\Delta t = 0.0026685$ fs. It is important to point out here that the value of N_λ ($\equiv \frac{\lambda}{h}$) is equal to 84.3744 according to the investigated wavelength $\lambda = 632.8$ nm and the grid spacing $h = 7.4999$ nm. According to Fig. 12, the predicted accuracy is expected to be very high since N_λ has a magnitude much larger than 3.1. The total field is discretized uniformly, leading to a mesh with $121 \times 121 \times 121$ grids. The predicted results for E_z are plotted at the cutting plane $z = 0$ nm in Fig. 20. We also consider the effect of the number of scatters by increasing the cylinder number of from one to four schematically shown in Fig. 21. The three-dimensional results predicted in the domain with the same grid resolution as the case with a single cylinder are plotted for E_z at the cutting plane $z = 0$ nm. For the sake of completeness, we also conduct grid-independent study by comparing the solutions plotted in Figs. 22 and 23 at different grid resolutions. One can see two solutions computed at 121^3 and 141^3 meshes agree well with each other, thereby confirming the computation of grid-independent solutions.

7.2. L-shaped photonic crystal waveguide problem

A lattice of many finite-length vertical rods (dielectric pillars) in a domain containing the L-shaped defect channel is investigated. The relative electric permittivity of the medium surrounding the uniformly distributed pillars is assumed to be 1, while the dielectric constant of the pillars is set at $\varepsilon_r = 11.56$. The waveguide of width $\frac{w}{a} = 2$ is constructed by taking one

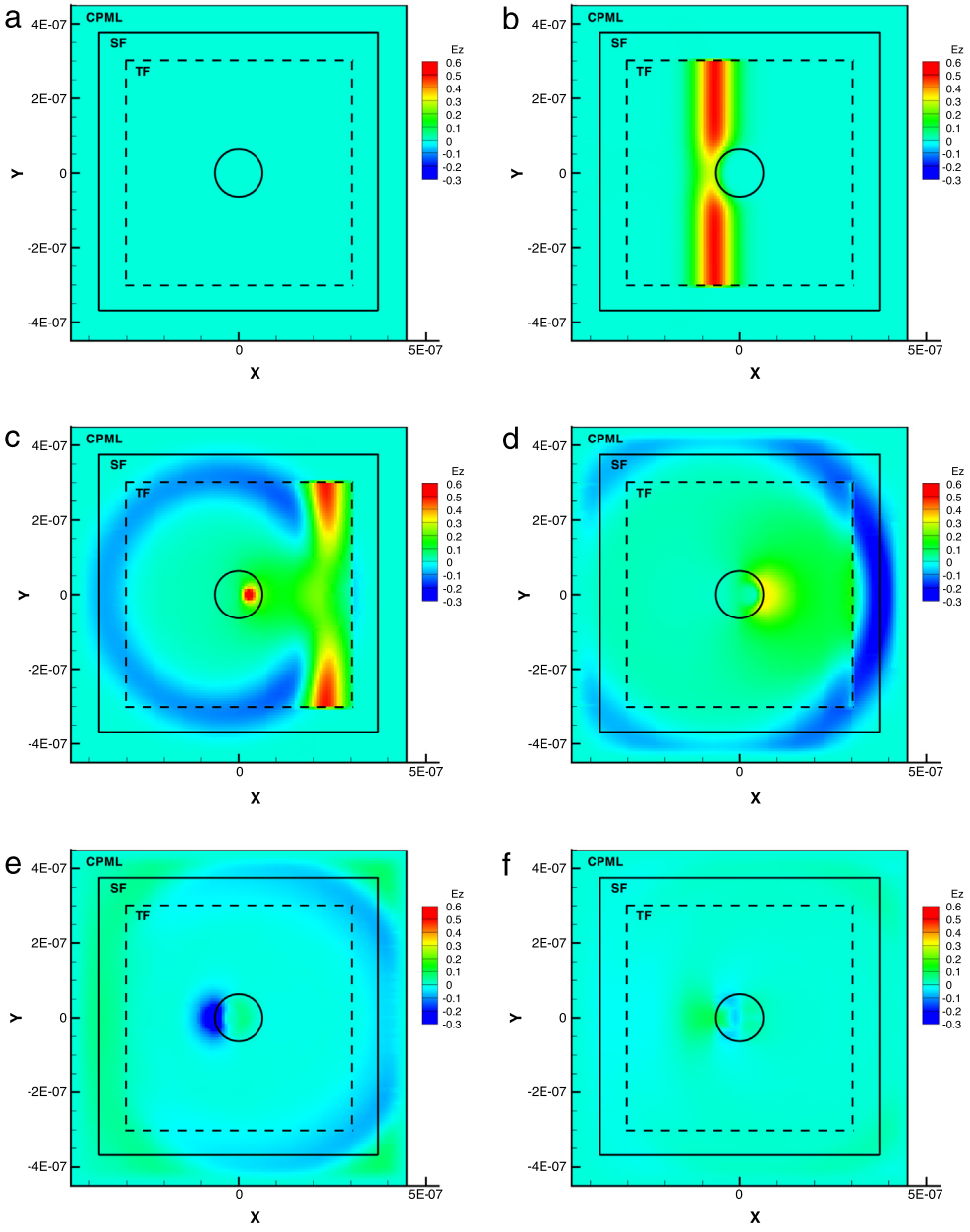

Fig. 20. The predicted contours of E_z ($z = 0$) at the cutting plane containing the cylindrical scatter. (a) Time step $=$ 0 (0 fs); (b) time step $=$ 560 (2.8 fs); (c) time step $=$ 760 (3.8 fs); (d) time step $=$ 850 (4.25 fs); (e) time step $=$ 1160 (5.8 fs); (f) time step $=$ 1800 (9 fs). Note that the grid numbers in the domains of TF, TF $\bigcup$ SF and TF $\bigcup$ SF $\bigcup$ CPML are $81 \times 81 \times 81$, $101 \times 101 \times 101$, and $121 \times 121 \times 121$, respectively.

vertical and one row pillars away, thereby leading to a three-dimensional L-shaped defect channel. A light of the frequency belonging to the photonic band gap is under our investigation. The radius of the investigated pillars is chosen as $0.2a$, where the lattice constant a (=515 nm) denotes the length between the centroids of two adjacent pillars.

The L-shaped bent waveguide problem is simulated at $\Delta t = 0.05337$ fs and $\Delta x = \Delta y = \Delta z = 57.1429$ nm. The number of grid points is $141 \times 141 \times 141$. The convolutional PML is attached to the scatter field to absorb *EM* wave and thus to effectively reduce unphysical wave that may re-enter into the domain. Fig. 24 shows the E_z contours for the case computed at the normalized frequency $= 0.353$ ($\frac{c}{a}$) (or wavelength $= 1458.92$ nm), where c denotes the speed of light. In this case, the wavelength λ of the incident wave is 1458.92 nm and the chosen grid spacing h is 57.1429 nm. The resulting value of N_λ ($\equiv \frac{\lambda}{h}$) is 25.5311, which is much larger than 5. The optical wave is seen to propagate through a ninety degree bend and the electric field is concentrated mostly in this defect channel. In Fig. 25, the current three-dimensional result in the L-shaped defect channel is compared with the two-dimensional result of Mekis et al. [41].

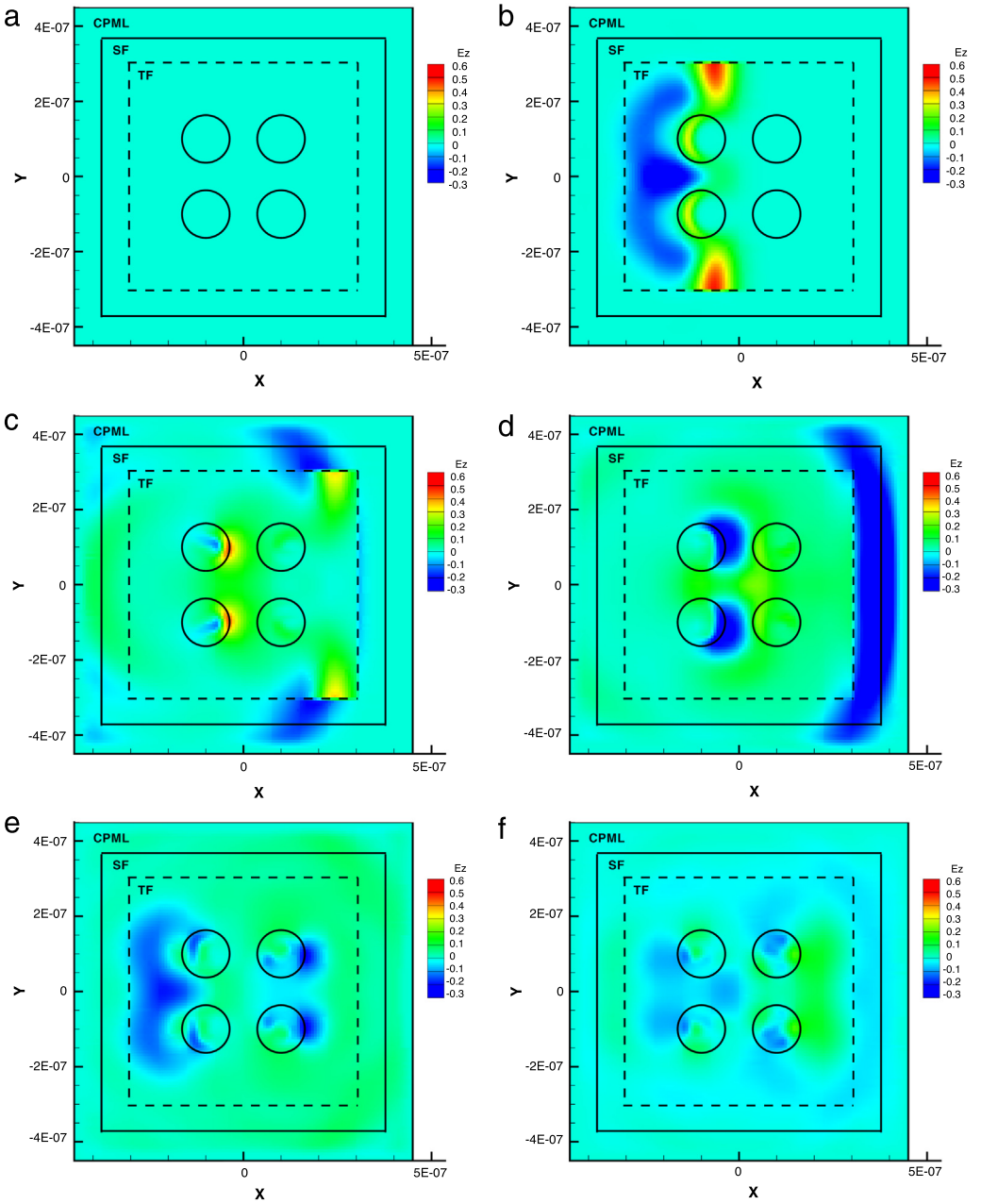

Fig. 21. The predicted contours of E_z ($z = 0$) at the cutting plane containing four cylindrical scatters. (a) Time step $=$ 0 (0 fs); (b) time step $=$ 560 (2.8 fs); (c) time step $=$ 760 (3.8 fs); (d) time step $=$ 850 (4.25 fs); (e) time step $=$ 1160 (5.8 fs); (f) time step $=$ 1800 (9 fs). The number of grid points employed in this calculation is identical to those in Fig. 20.

8. Numerical results in Drude medium

In the one dimensional domain, the left half involves the vacuum and the right half contains the Drude media. Each half of the domain has been divided into the 250 uniform intervals of the length $\Delta x = 7.5 \times 10^{-5}$ m. Two perfect matching layers of length $10\Delta x$ are attached to both ends so as to be able to absorb the possibly reflected wave.

A Gaussian pulse at $x = 125\ \Delta x$ has the form $\exp[-(\frac{t-t_0}{d})^2]$, where $d = 40\ \Delta t$, $t_0 = 120\ \Delta t$, and $\Delta t = 0.125 \times 10^{-12}$ s. The parameters of the Drude medium on the right-half of the domain are chosen to be $\varepsilon_\infty = 1, f_p = 28.7$ GHz, $\omega = 2\pi f_p$, $\gamma_p = 20$ GHz. The computed value of Ez is plotted with respect to time at the monitoring point 489 Δx. One can clearly see that the result plotted in Fig. 26 agrees well with the referenced solutions [42], thereby validating the proposed numerical method.

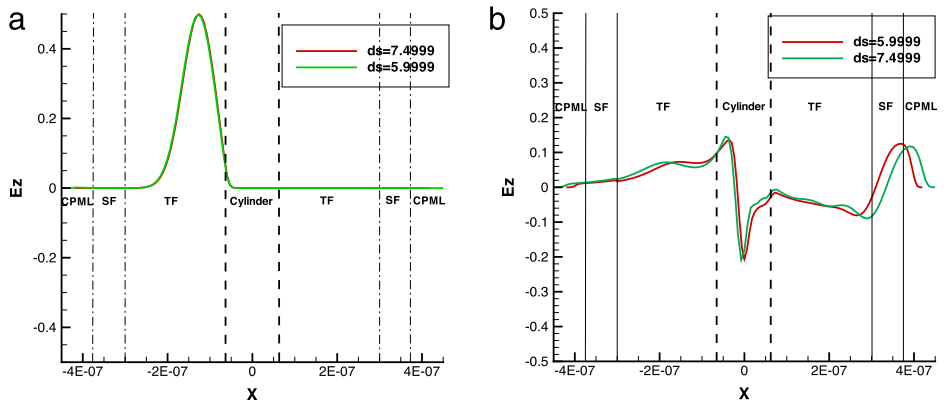

Fig. 22. Comparison of the computed profiles of E_z $(x,\ y = 0,\ z = 0)$ in grids 121^3 and 141^3. (a) $t = 2.601$ fs; (b) $t = 5.253$ fs.

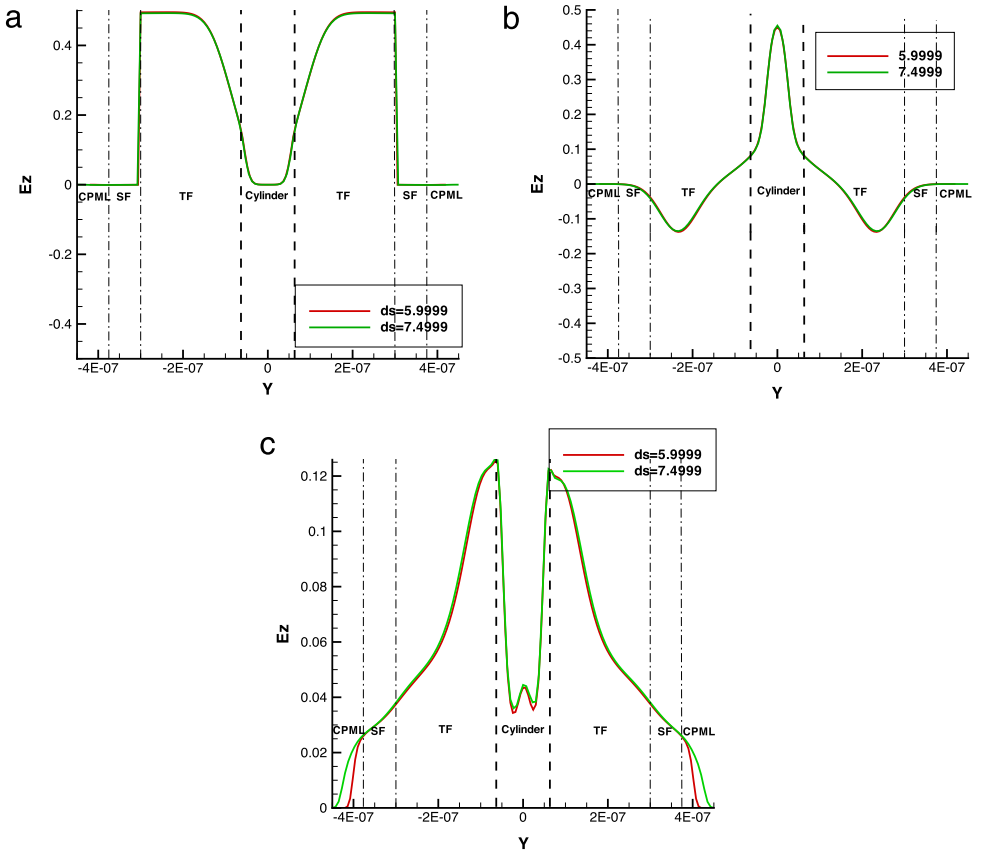

Fig. 23. Comparison of the computed profiles of E_z $(x = 0,\ y,\ z = 0)$ in grids 121^3 and 141^3. (a) $t = 3.002$ fs; (b) $t = 3.552$ fs; (c) $t = 4.503$ fs.

For the 3D case [43], a mesh $44 \times 44 \times 44$ grids is distributed uniformly in the region of interest and 10-cell CPMLs are attached on the six sides of the lattice. The parameters of the Drude medium are chosen to be $\varepsilon_\infty = 1, f_p = 2.87$ GHz, $\omega = 2\pi f_p, \gamma_p = 200$ GHz. The electric dipole located at the center of the computational region is a Gaussian pulse, which is expressed as

$$P(t) = 10^{-10} \exp\left[-\left(\frac{t - t_0}{\tau}\right)^2\right] \tag{27}$$

where $\tau = 2 \times 10^9, t_0 = 3\tau$.

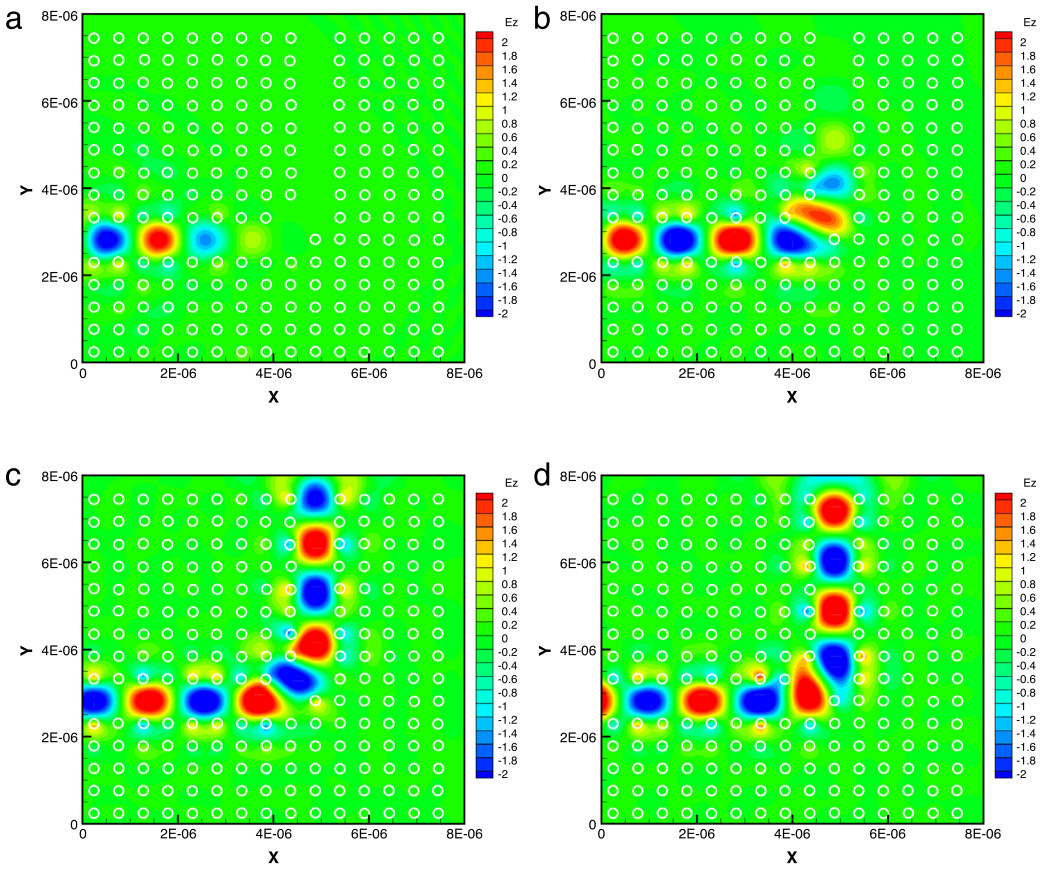

Fig. 24. The predicted contours of E_z at the cutting plane ($z = 0$). (a) Time step $=$ 575 (30.68775 fs); (b) time step $=$ 1075 (57.37275 fs); (c) time step $=$ 1750 (93.3975 fs); (d) time step $=$ 2325 (124.08525 fs).

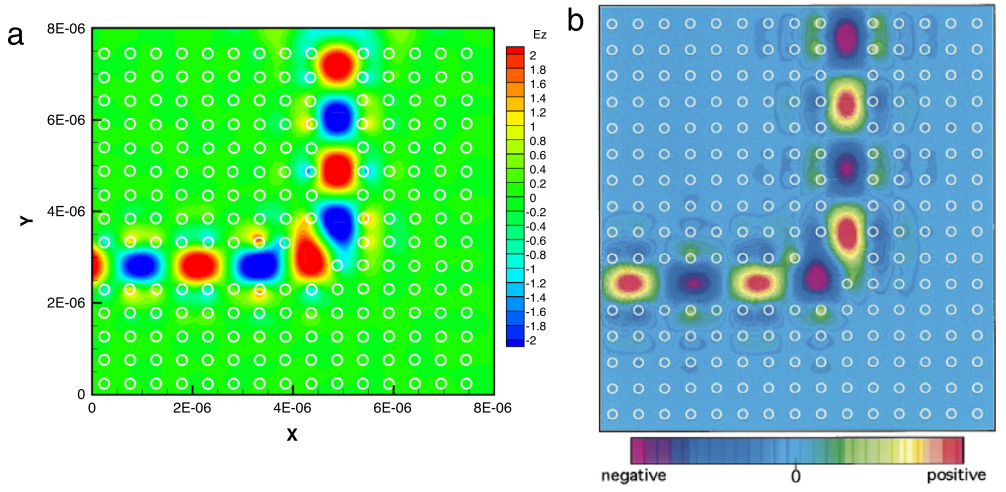

Fig. 25. Snapshot of the computed E_z field values at the time step 2325 (or $t = 124.08525$ *fs*) in the L-shaped waveguide at the normalized frequency $0.353(c/a)$. (a) Present; (b) Mekis et al. [41].

The reference solution $E_{ref}|^n_{i,j,k+\frac{1}{2}}$ is considered at the grid location $(i, j, k + \frac{1}{2})$ and at the time-step n. This reference solution is obtained in a larger domain with $200 \times 200 \times 200$ grid points. The field-observation points are chosen at P (two cells away from the adjacent absorbing boundary), Q (two cells away from the two adjacent absorbing boundaries), and R (two cells away from the three adjacent absorbing boundaries in the corner) schematically shown in Fig. 27. The relative

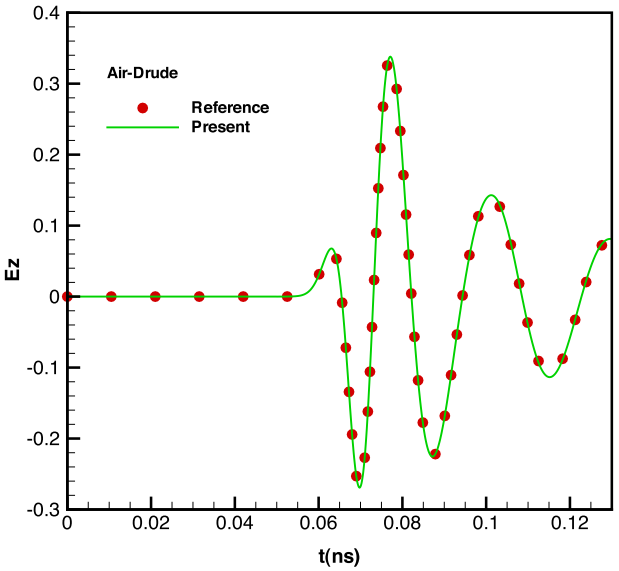

Fig. 26. Comparison of computed and Ref. [42] electromagnetic wave (E_z field) solutions in the domain including both of the vacuum and Drude medium.

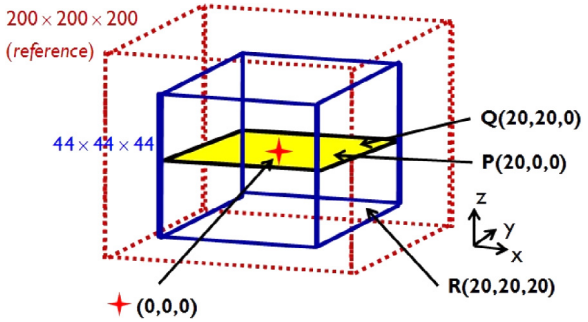

Fig. 27. Schematic of the 3D domain containing the Drude medium. Note that the small and large boxes denote the physical and the reference domains, respectively.

error is defined as

$$Relative\ error|^{n}_{i,j,k+\frac{1}{2}} = \frac{\left|E|^{n}_{i,j,k+\frac{1}{2}} - E_{ref}|^{n}_{i,j,k+\frac{1}{2}}\right|}{\left|E_{refmax}|^{n}_{i,j,k+\frac{1}{2}}\right|} \tag{28}$$

where $E_{refmax}|^{n}_{i,j,k+\frac{1}{2}}$ is the maximum amplitude of the reference field at $(i, j, k+\frac{1}{2})$. One can observe from Fig. 28((a)–(c)) that the computed solutions match well with the reference solutions at the points P, Q and R. Also, the reflected solutions are negligibly small, thereby justifying the proper use of the CPML to absorb the outgoing wave.

9. Concluding remarks

Three-dimensional Maxwell's equations have been solved in dispersive and non-dispersive media using the developed FDTD scheme in staggered grids. Our aim is to numerically preserve symplecticity and conserve Hamiltonian and invariants all the time for the ideal Maxwell's equations. To achieve these objectives, the explicit symplectic partitioned Runge–Kutta time integrator is applied together with the space-centered spatial scheme. To increase the phase accuracy, the difference between the numerical and exact phase velocities is minimized. The proposed temporal second-order and spatial fourth-order accurate three-dimensional scheme developed in staggered grids for Maxwell's solutions are shown to have a better performance when compared with other referenced schemes. Several exact and benchmark problems have been solved for the purposes of verification and validation and all the predicted solutions have been shown to agree well with the exact and the benchmark numerical solutions.

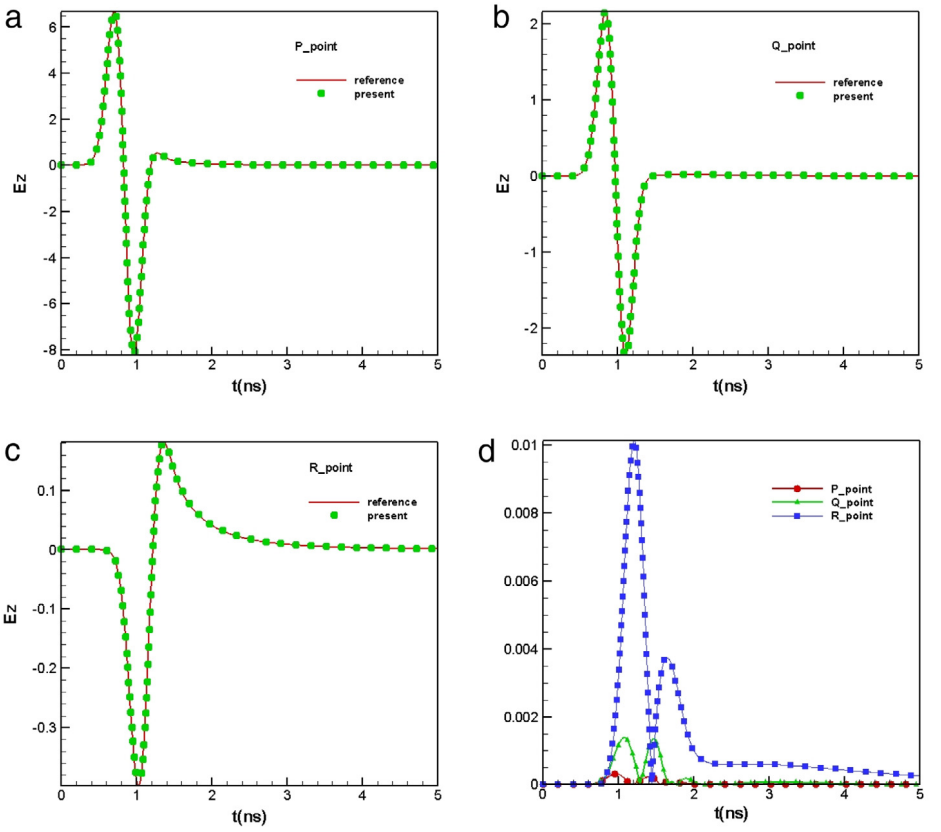

Fig. 28. The predicted E_z values and the computed relative errors at P, Q and R points in the $44 \times 44 \times 44$ and the $200 \times 200 \times 200$ cells. (a) The E_z value at point P; (b) the E_z value at point Q; (c) the E_z value at point R; (d) the predicted relative errors.

Acknowledgment

This work was supported by the National Science Council of the Republic of China under the Grants NSC96-2221-E-002-293-MY2, NSC96-2221-E-002-004, and CQSE97R0066-69.

References

[1] J.X. Cai, Y.S. Wang, B. Wang, B. Jiang, New multisymplectic self-adjoint scheme and its composition scheme for the time-domain Maxwell's equations, J. Math. Phys. 47 (2006) 1–18.
[2] K.S. Yee, Numerical solution of initial boundary value problems involving Maxwell's equations in isotropic media, IEEE Trans. Antennas and Propagation 14 (1960) 302–307.
[3] C.-D. Munz, P. Ommes, R. Schneider, E. Sonnendrücker, U. Voß, Divergence correction techinques for Maxwell solvers based on a hyperbolic model, J. Comput. Phys. 161 (2000) 484–511.
[4] B. Cockburn, F. Li, C.-W. Shu, Locally divergence-free discontinuous Galerkin methods for the Maxwell equations, J. Comput. Phys. 194 (2004) 588–610.
[5] B. Zhu, J. Chen, W. Zhong, Q.H. Liu, A hybrid FETD-FDTD method with nonconforming meshes, Commun. Comput. Phys. 9 (2011) 828–842.
[6] T.T. Zygiridis, T.D. Tsiboukis, Optimized three-dimensional FDTD discretizations of Maxwell's equations on Cartesian grids, J. Comput. Phys. 226 (2007) 2372–2388.
[7] S. Caorsi, G. Cevini, Assessment of the performances of first and second-order time-domain ABC's for the truncation of finite element grids, Microw. Opt. Technol. Lett. 38 (1) (2003) 11–16.
[8] D. Jiao, M. Lu, E. Michielssen, J.M. Jin, A fast time domain finite element-boundary integral method for electromagnetic analysis, IEEE Trans. Antennas and Propagation 49 (10) (2001) 1453–1461.
[9] J. Berenger, A perfectly matched layer for the absorption of electromagnetic waves, J. Comput. Phys. 114 (2) (1994) 185–200.
[10] W.C. Chew, W.H. Weedon, A 3D perfectly matched medium from modified Maxwell's equations with stretched coordinates, Microw. Opt. Technol. Lett. 7 (1994) 599–604.
[11] Z.S. Sacks, D.M. Kingsland, R. Lee, J.F. Lee, A perfectly matched anisotropic absorber for no as an absorbing boundary condition, IEEE Trans. Antennas and Propagation 43 (12) (1995) 1460–1463.
[12] M. Kuzuoglu, R. Mittra, Frequency dependence of constitutive parameters of casual perfectly matched anisotropic absorbers, IEEE Microw. Guid. Wave Lett. 6 (12) (1996) 447–449.
[13] S. Wang, R. Lee, F.L. Teixira, Anisotropic-medium PML for vector FETD with modified basis functions, IEEE Trans. Antennas and Propagation 54 (1) (2006) 20–27.
[14] S. Lanteri, C. Scheid, Convergence of a discontinuous Galerkin scheme for the mixed time-domain Maxwell's equations in dispersive media, IMA J. Numer. Anal. 33 (2013) 432–459.
[15] H.T. Banks, V.A. Bokil, N.L. Gibson, Analysis of stability and dispersion in a finite element method for Debye and Lorentz dispersive media, Numer. Methods Partial Differential Equations 25 (2009) 885–917.

[16] V.A. Bokil, N.L. Gibson, Analysis of spatial high-order finite difference methods for Maxwell's equations in dispersive media, IMA J. Numer. Anal. 32 (3) (2012) 926–956.
[17] Li. Jichun, Unified analysis of leap-frog methods for solving time-domain Maxwell's equations in dispersive media, J. Sci. Comput. 47 (2011) 1–26.
[18] Li. Jichun, Error analysis of fully discrete mixed finite element schemes for 3-d Maxwell's equations in dispersive media, Comput. Methods Appl. Mech. Engrg. 196 (2007) 3081–3094.
[19] J.A. Roden, S.D. Gedney, Convolution PML (CPML): An efficient FDTD implementation of the CFS-PML for arbitrary media, Microw. Opt. Technol. Lett. 27 (2000) 334–339.
[20] N. Anderson, A.M. Arthurs, Helicity and variational principles for Maxwell's equations, Int. J. Electron. 54 (1983) 861–864.
[21] J.E. Marsden, A. Weinstein, The Hamiltonian structure of Maxwell–Vlasov equations, Phys. D 4 (1982) 394–406.
[22] J.U. Brackbill, D.C. Barnes, The effect of nonzero product of magnetic gradient and B on the numerical solution of the magnetohydrodynamic equations, J. Comput. Phys. 35 (1980) 426–430.
[23] L.D. Landau, E.M. Lifshitz, L.P. Pitaevskii, Electrodynamics of Continuous Media, Pergamon Press, Oxford, 1984.
[24] B. Jiang, J. Wu, L.A. Povinelli, The origin of spurious solutions in computational electromagnetics, NASA-TM-10692, E-9633, ICOMP-95-8, 1995.
[25] F. Assous, P. Degond, E. Heintze, P.A. Raviart, J. Serger, On a finite-element method for solving the three-dimensional Maxwell equations, J. Comput. Phys. 109 (1993) 222–237.
[26] J.M. Sanz-Serna, Symplectic Runge–Kutta and related methods: recent results, Physica D (1992) 293–302.
[27] L.L. Jiang, J.F. Mao, X.L. Wu, Symplectic finite-difference time-domain method for Maxwell equations, IEEE Trans. Antennas and Propagation 42 (8) (2006) 1991–1995.
[28] W. Chen, X. Li, D. Liang, Symmetric energy-conserved splitting FDTD scheme for the Maxwell's equations, Commun. Comput. Phys. 6 (2009) 804–825.
[29] L. Gao, D. Liang, New energy-conserved identities and super-convergence of the symmetric EC-S-FDTD scheme for Maxwell's equations in 2D, Commun. Comput. Phys. 11 (2012) 1673–1696.
[30] W. Sha, Z.X. Huang, M.S. Chen, X.L. Wu, Survey on symplectic finite-difference time-domain schemes for Maxwell's equations, IEEE Trans. Antennas and Propagation 56 (2008) 493–510.
[31] P.G. Petropoulos, Stability and phase error analysis of FD-TD in dispersive dielectrics, IEEE Trans. Antennas and Propagation 42 (1994) 62–69.
[32] A. Taflove, M.E. Brodwin, Numerical solution of steady-state electromagnetic scattering problems using the time-dependent Maxwell's equations, IEEE Trans. Microw. Theory Tech. 23 (1975) 623–630.
[33] U.M. Ascher, R.I. McLachlan, Multisymplectic box schemes and the Korteweg–de Vries equation, Appl. Numer. Math. 48 (2004) 255–269.
[34] Y. Sun, P.S.P. Tse, Symplectic and multisymplectic numerical methods for Maxwell's equations, J. Comput. Phys. 230 (2011) 2076–2094.
[35] L.N. Trefethen, Group velocity in finite difference schemes, SIAM Rev. 24 (1982) 113–136.
[36] L. Gao, B. Zhang, D. Liang, The splitting finite-difference time-domain methods for Maxwell's equations in two dimensions, J. Comput. Appl. Math. 205 (2007) 207–230.
[37] T. Hagstrom, S. Lau, Radiation boundary conditions for Maxwell's equations: A review of accurate time-domain formations, J. Comput. Math. 25 (2007) 305–336.
[38] A. Taflove, S.C. Haguess, Computational Electrodynamics: The Finite-Difference Time-Domain Method, third ed., Artech House, 2005.
[39] S.D. Gedney, An anisotropic perfectly matched layer absorbing media for the truncation of FDTD lattices, IEEE Trans. Antennas and Propagation 44 (1996) 1630–1639.
[40] J.A. Roden, S.D. Gedney, Convolution PML (CPML): An efficient FDTD implementation of the CFS-PML for arbitrary media, Microw. Opt.Technol. Lett. 27 (2000) 334–338.
[41] A. Mekis, J.C. Chen, I. Kurland, S. Fan, P.R. Villeneuve, J.D. Joannopoulos, High transmission through sharp bends in photonic crystal waveguides, Phys. Rev. Lett. 77 (1996) 3787–3790.
[42] B. Wei, X.Y. Li, F. Wang, D. Liang, The splitting finite-difference time-domain methods for Maxwell's equations in two dimensions, J. Comput. Appl. Math. 205 (2007) 207–230.
[43] B. Wei, X.Y. Li, F. Wang, D. Liang, A novel UPML FDTD absorbing boundary condition for dispersive media, Waves Random Complex 20 (3) (2010) 511–527.